OEA | Opto-Electronic Advances

Review

June 2026, Vol. 9, No. 6

Open Access

# Emerging optical techniques for sorting and detection of chiral particles

Yuzhi Shi[1,2,3,4,5,6,7*†], Chengfeng Li[4,5,6,7†], Xiaolei Lin[1,2,3†], Wenwen Xue[1,2,3†], Chengxing Lai[4,5,6,7], Tao He[4,5,6,7], Qinghua Song[8], Zhanshan Wang[4,5,6,7], Yulan Wang[1,2,3*], Din Ping Tsai[9*], Xinbin Cheng[4,5,6,7*] and Haidong Zou[1,2,3*]

**Abstract:** Sorting and detection of enantiomers hold critical importance in biomedical, chemical, and pharmacological sciences due to their fundamental role in molecular interactions and therapeutic efficacy. Over the past two decades, diverse chemical, biophysical, and microfluidic methodologies have been developed for chiral enantiomer sorting and detection. While these approaches have demonstrated significant capabilities, optical techniques have attracted increasing interest due to their intrinsic advantages, including rapid analysis, minimal sample consumption, and non-invasive operation. This review comprehensively overviews recent advances in optical methods for chiral enantiomer sorting and detection. We focus on emerging optical concepts, including exotic optical forces and engineered light fields, such as bound states in the continuum and metasurfaces, and analyze their operational principles, capabilities, and inherent limitations. Furthermore, we investigate the growing impact of artificial intelligence in reshaping optical sorting and sensing strategies, particularly its role in improving analytical precision and enabling autonomous operation. The review concludes with a forward-looking perspective, discussing persistent challenges like system scalability and real-world implementation while outlining promising future directions, including integrated lab-on-chip platforms and advanced chiral metamaterials.

**Keywords:** chiral molecules; optical sorting; optical detection; artificial intelligence; biochemical applications

DOI: 10.29026/oea.2026.250255 | CSTR: 32247.14.oea.2026.250255

**Citation:** Shi YZ, Li CF, Lin XL et al. Emerging optical techniques for sorting and detection of chiral particles. *Opto-Electron Adv* **9**, 250255 (2026).

## 1 Introduction

Chiral molecules, existing as non-superimposable mirror images (enantiomers), are fundamental building blocks of life and pervasive throughout nature and technology[1,2]. Their significance stems from the profound fact that enantiomers often exhibit drastically different biological, chemical, and physical properties. In pharmaceuticals, one enantiomer may be a life-saving drug while its mirror image could be inactive or even toxic[3]. In agrochemicals, enantiomeric purity dictates pesticide effectiveness and environmental safety. In biology, the homochirality of amino acids and sugars (L- and D-forms, respectively) is essential for the structure and function of proteins, DNA, and cellular processes[4]. Furthermore, chiral molecules play vital roles in flavours, fragrances, and as components in advanced materials like liquid crystals[5] and catalysts. Consequently, the ability to detect and separate chiral molecules is indispensable across diverse fields, including medicine[6], biochemistry[7], pharmacology[8], materials science[9], and food science[10].

Received: 23 September 2025

Accepted: 20 January 2026

Published online: 24 March 2026

[1]Shanghai Eye Diseases Prevention & Treatment Center/Shanghai Eye Hospital, School of Medicine, Tongji University, Shanghai 200092, China; [2]National Clinical Research Center for Eye Diseases, Shanghai 200080, China; [3]Shanghai Engineering Center for Precise Diagnosis and Treatment of Eye Diseases, Shanghai 200080, China; [4]Institute of Precision Optical Engineering, School of Physics Science and Engineering, Tongji University, Shanghai 200092, China; [5]MOE Key Laboratory of Advanced Micro-Structured Materials, Shanghai 200092, China; [6]Shanghai Institute of Intelligent Science and Technology, Tongji University, Shanghai 200092, China; [7]Shanghai Frontiers Science Center of Digital Optics, Shanghai 200092, China; [8]Tsinghua Shenzhen International Graduate School, Tsinghua University, Shenzhen 518055, China; [9]Department of Electrical Engineering, City University of Hong Kong, Kowloon, Hong Kong SAR 999077, China.

[†]These authors contributed equally to this work.

*Correspondence: YZ Shi, E-mail: yzshi@tongji.edu.cn; YL Wang, E-mail: shybfzs@163.com; DP Tsai, E-mail: dptsai@cityu.edu.hk; XB Cheng, E-mail: chengxb@tongji.edu.cn; HD Zou, E-mail: zouhaidong@sjtu.edu.cn

Non-optical techniques offer diverse approaches for sorting and detecting chiral molecules. Chromatography[11–13], particularly using chiral stationary phases (CSPs), serves as a cornerstone, where enantiomers are separated based on differential interactions with immobilized chiral selectors (such as cyclodextrins and proteins) within a column, resulting in distinct retention times. Capillary electrophoresis achieves high-resolution separation by incorporating chiral additives into the buffer, exploiting differences in electrophoretic mobility. Crystallization-based methods[14,15], such as classical resolution via diastereomeric salt formation, leverage disparities in solubility or crystallization kinetics between enantiomerically pure compounds or their diastereomeric derivatives. For the detection, approaches include enzymatic assays, electrochemical sensors, immunoassays, and colorimetric methods. However, these non-optical methods could generally suffer from several limitations, including the need for sample derivatization (e.g., for colorimetry or diastereomer formation), destructive analysis, limited throughput, high cost, and system complexity. These limitations highlight the demand for advanced optical techniques[16,17], such as optical forces, polarimetry, circular dichroism (CD) spectroscopy, and so forth. These optical methods provide non-destructive analysis, real-time monitoring capabilities, higher potential throughput, and normally require minimal sample preparation, offering a vital alternative for comprehensive chiral analysis.

Despite sustained progress, chiral separation and detection remain fundamentally challenging from a physical perspective. The intrinsic weakness of chiroptical interactions, which typically arising from electromagnetic dipole coupling, severely limits enantioselectivity and signal strength. For optical sorting, generating sufficiently strong and selective chiral optical forces is nontrivial due to their subtle dependence on field helicity, momentum, and near field gradients. For optical detection, reliably distinguishing weak chiral signatures from background remains a central bottleneck, particularly at low concentrations. These theoretical and practical challenges have motivated the rapid development of engineered light fields, nanophotonic platforms, and artificial intelligence (AI)-assisted strategies, which together form the core focus of this review.

While numerous reviews have summarized developments in chiral optical sensing and chiral-light interactions in recent years[18–20], most were published over five years ago and thus miss significant recent advances. Concurrently, optical sorting of chiral molecules has attracted substantial attention, generating numerous novel approaches that now stimulate a comprehensive review. Motivated by these factors, we herein provide a comprehensive review of the optical sorting and detection of chiral molecules. Specifically, we focus on the recent advances and newly emerged optical techniques. We discuss various platforms for optical sorting, including both far-field and near-field systems. These systems enable the exploration of new physical phenomena. Meanwhile, novel techniques have emerged for the optical detection of a great diversity of chiral molecules.

### 1.1 Overview of optical sorting and detection of chiral particles

This review first offers a brief introduction to established non-optical techniques for chiral sorting and detection, such as chemical, biophysical, and microfluidic methods. We highlight their essential characteristics and principal limitations, whereas in-depth analyses are available in other dedicated reviews. Next, two major areas of this paper will be explored, namely, optical sorting and detection of chiral particles. We introduce the underlying physics, platforms, and techniques in these two areas. The feasibility and limitations of various approaches are also compared and examined, which may handle specific types of chiral molecules. We note that there are some ongoing issues that need to be solved shortly. Thus, the review concludes with a discussion of future prospects for these two rapidly growing and promising research fields.

### 1.2 Milestones of optical sorting and detection of chiral particles

The backbone of this paper is illustrated in Fig. 1. Platforms for the optical sorting include single interfaces, metasurfaces[21–23], vector beams[24], slot waveguides, optofluidics[25,26], etc. New physics and ideas can be explored using these platforms. Notable examples include the bound state in the continuum (BIC)[27], exceptional point (EP)[28,29], interference fields, multipoles[30] and toroidals[31]. Specifically, the optical sorting relies on the generation of optical forces, ranging from conventional to exotic ones. Recent detection techniques for the detection of chiral molecules mainly focus on engineering superchiral light fields, which can be configured through various designs, such as nanocavities, metasurfaces, plasmonics[32], and surface-enhanced Raman scattering (SERS)[33]. Specific chiral molecules can also be probed in a complex sample via machine learning (ML)[34,35]. The advances of those techniques have enabled the detection of numerous chiral molecules, including synthesized metallic nanoparticles, complex-shaped ones, particle-biomolecule complexes, chemical molecules, and biomolecules.

The milestones for optical sorting and detection are plotted in Fig. 2. The history of optical sorting dates back to 2013, when Tkachenko et al. proposed the idea to utilize the optical radiation pressure (ORP) for sorting chiral particles[36]. Experiments of optical sorting using the optical gradient force (OGF) were reported in 2014[37]. The optical lateral force (OLF) represents a typical force transverse to the light propagation direction and has no contributions from light gradients. This force was born with strong capabilities for sorting with left- and right-handedness chiral particles in 2014[38]. Much later, in 2019, Kravets et al.

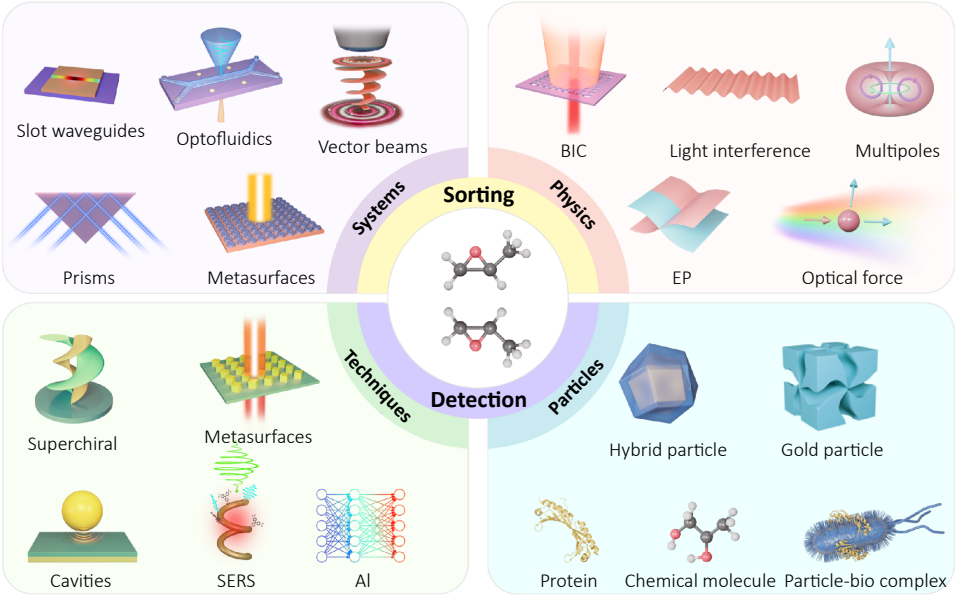



Fig. 1 | Schematic overview of optical chirality research. The diagram is divided into four conceptual sections. The top-left section illustrates representative systems for optical sorting, including slot waveguides, optofluidics, vector beams, prisms, and metasurfaces. The bottom-left section presents emerging techniques for chiral detection, such as superchiral fields, metasurfaces, nanocavities, SERS, and AI-assisted approaches. The top-right section highlights underlying physical mechanisms for optical sorting, including BICs, EPs, light interference, and multipolar responses. The bottom-right section depicts typical chiral targets in optical detection, such as bioparticles and synthesized chiral nanoparticles.

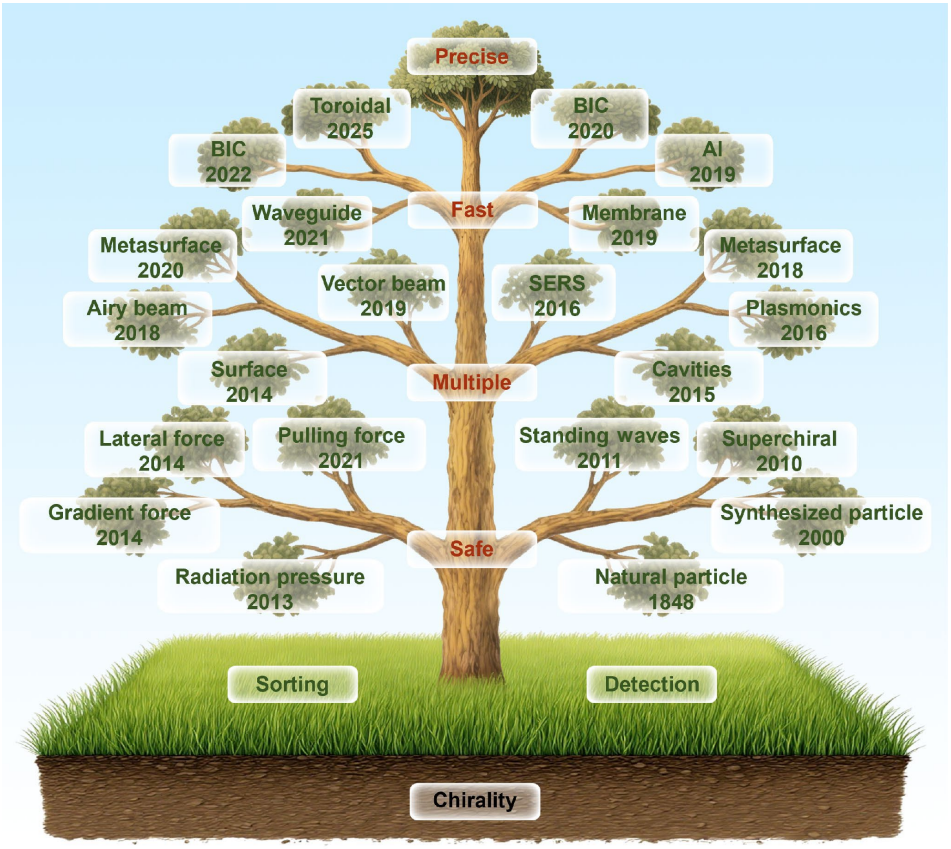



Fig. 2 | Chiral tree for the timeline of key milestones in optical sorting and detection. The left panel highlights the development of optical sorting, from early demonstrations of radiation pressure to gradient forces, lateral forces, and pulling forces, and more recent approaches involving structured beams, waveguides, and metasurfaces. The right panel summarizes advances in optical detection, from early circular dichroism of natural and synthesized chiral particles and the introduction of superchiral fields to plasmonics, nanocavities, metasurfaces, and AI-assisted chiral sensing.

reported the chiral optical Stern-Gerlach Newtonian experiment, which can be utilized for optical sorting[39]. Though the optical pulling force (OPF) was proposed earlier than the OLF, early-stage sorting applications using the OPF mainly focus on achiral particles[40]. In 2021, Ali et al. used the OPF for sorting chiral particles[41].

Leveraging those forces, various light fields and mechanisms have been used for chiral sorting. Notable examples include the surface-based sorting in 2014[38], Airy beam in 2018, vector beam in 2019[42], metasurface in 2020[17], waveguide in 2021[43], BIC in 2022[44], and toroidals in 2025[45].

For the optical detection, the earliest works addressing natural and synthesized chiral particles date back to 1848[46] and 2000[47], respectively. In the early stage, circularly polarized light with limited optical chirality was used for the detection, resulting in limited sensitivity. In 2010, Hendry et al. achieved the ultrasensitive detection of biomolecules using superchiral fields[48]. After that, numerous approaches have been adopted for the generation of superchiral light. For instance, chiral particles can be detected using standing waves in 2011[49], nanocavities in 2015[50], plasmonics in 2016[51], SERS in 2016[52], metasurface in 2018[53], membrane in 2019[54], AI in 2019[55], and BIC in 2020[56]. With the advances of nanophotonics, current techniques have achieved a remarkable sensitivity down to $10^{-15}$ M[57].

## 2 Chiral sorting

### 2.1 Non-optical techniques for chiral sorting

Before delving into optical strategies for chiral sorting, it is instructive to briefly survey the diverse chemical, biophysical, and microfluidic methodologies that have been traditionally employed for enantioseparation. Considering that the present review primarily focuses on optical technologies, we provide here only a brief overview of non-optical methods. More comprehensive discussions can be found in various review papers[58–70].

Traditional chemical chiral molecular separation encompasses a variety of techniques, primarily including chromatography[11–13], crystallization and kinetic resolution[14,15], membrane-based enantioseparation techniques[71–73], adsorption and fixed-bed processes, as well as emerging synergistic methods[13,74,75].

Chromatography remains the most established strategy for enantioseparation. It includes high-performance liquid chromatography (HPLC)[11], gas chromatography (GC), capillary electrophoresis (CE)[76], and supercritical-fluid chromatography (SFC)[77], all of which exploit CSPs for enantiomeric resolution. HPLC is the most widely used, but its application is limited by high solvent consumption, costly CSPs, and lengthy optimization[11,13]. GC works well for volatile and thermally stable compounds, but is constrained by the scarcity of chiral columns. SFC, a newer chiral separation technology employing $CO_2$ as the mobile phase, enables tunable polarity via temperature, pressure, or solvent modifiers (Fig. 3(a))[77]. It combines the high diffusivity of GC with the solubilizing capacity of HPLC to deliver efficient, rapid, and more sustainable separations. Recent efforts have primarily focused on developing novel CSPs with enhanced selectivity and broader applicability[78].

Beyond chromatography, crystallization provides a classical industrial approach for bulk production of single enantiomers. It relies on solubility differences and dynamic crystallization strategies to selectively enrich one enantiomer[14,15,79]. Complementarily, kinetic resolution employs chiral catalysts such as enzymes to preferentially convert one enantiomer from a racemic mixture, often coupled with rapid racemization to reach high enantiomeric excess[80].

Membrane-based strategies[81] offer a continuous and energy-efficient alternative. Chiral membranes constructed from frameworks such as Metal-Organic Frameworks (MOFs)[82], chiral Covalent Organic Frameworks (COFs) (Fig. 3(b))[71,74,83], and chiral nanosheets enable enantioselective transport. MOFs offer high surface area and tunable pore chemistry, while COFs provide superior chemical stability and uniform, scalable pores. Compared with chromatography, membrane-based processes deliver higher throughput and continuous operation, promising broad pharmaceutical applications.

In addition, emerging synergistic technologies are also gaining traction. Chiral aggregation-induced emission (AIEgen) aggregation-precipitation enables enantiomeric excess (ee) values up to 90% (Fig. 3(c))[84]. Electrochemical methods allow redox-controlled selective adsorption-desorption of enantiomers[85]. Chiral medium-entropy ceramics have further demonstrated stable and selective amino acids separation (Fig. 3(d))[86]. These approaches remain at an early stage but offer promising routes for high-throughput and green processes.

Although chemical and optical approaches dominate the field of enantioseparation, a smaller body of work has explored alternative strategies such as microfluidic and biological methods[70].

Microfluidic technology, as an interdisciplinary field integrating chemistry, fluid physics, and biomedical engineering, enables precise manipulation of nanoliter-to-attoliter fluids in microscale channels and chambers with the chip serving as the core functional carriers[87], as shown in Fig. 4(a). Various mechanisms have been developed for chiral separation[70]: electrophoretic mode[88] employs cross-channels and chiral selectors such as cyclodextrins to separate specially-labeled amino acids; chiral microvortex[89] regulation generates helical microvortices for racemic amino acids quantification via circular dichroism without chiral reagents; antisolvent crystallization[87] achieves complete chiral symmetry breaking (100% ee) in nanoliter volumes via coaxial capillaries; and the shear flow[90] mode efficiently separates helical bacteria in serpentine channels. Overall,

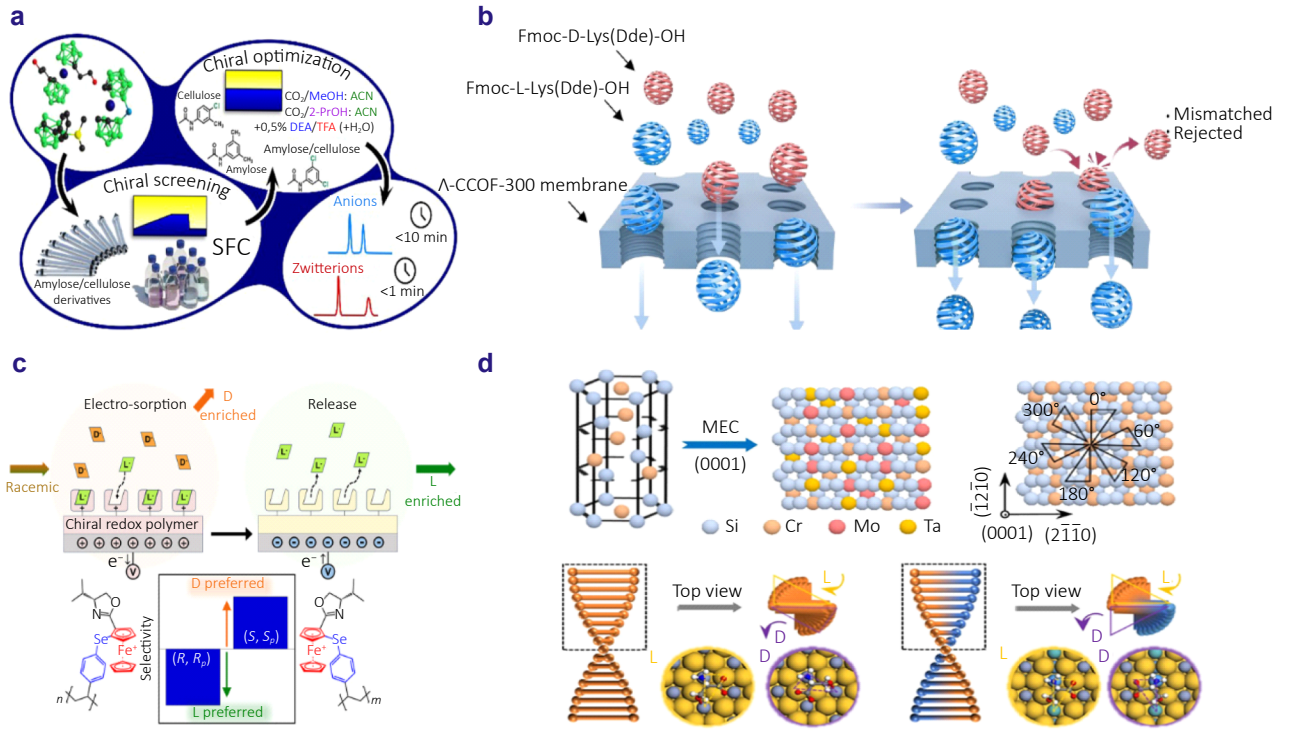



Fig. 3 | Representative chemical methods for enantioseparation. (a) Supercritical fluid chromatography with polysaccharide CSPs for efficient separation. (b) COFs-based membrane systems enabling size- and chiral-selective transport. (c) Redox-responsive planar-chiral metallopolymers enabling switchable enantioselective absorption. (d) Medium-entropy ceramics surfaces acting as chiral adsorbents via asymmetric binding energies. Figure reproduced with permission from: (a) ref.[77], American Chemical Society; (b) ref.[71], Springer Nature; (c) ref.[85], American Chemical Society; (d) ref.[86], Springer Nature.

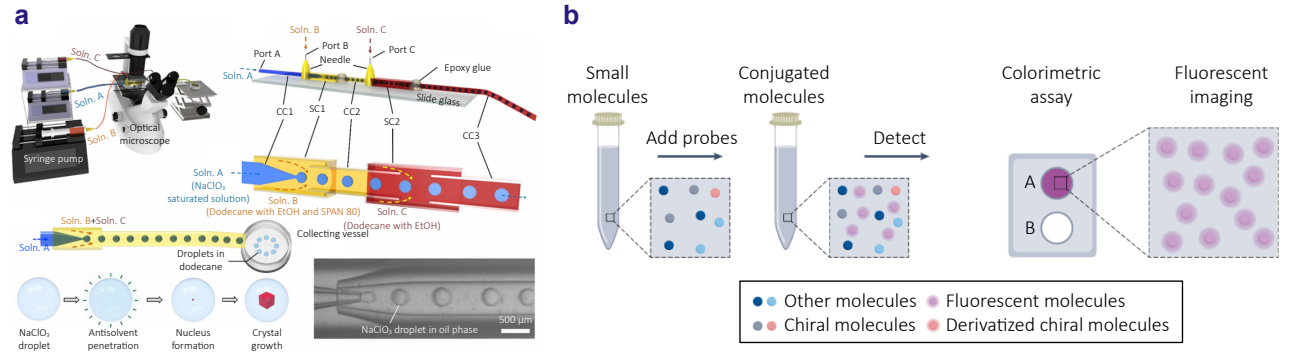



Fig. 4 | Alternative enantioseparation strategies: microfluidic and biological approaches. (a) Microfluidic platforms integrate antisolvent crystallization, offering high-throughput operation with minimal sample consumption. (b) Biological approaches employ enzymes, demonstrating highly selective recognition under mild and biocompatible conditions. Figure reproduced with permission from: (a) ref.[87], Royal Society of Chemistry; (b) ref.[70], Springer Nature.

microfluidics offers high speed, minimal sample consumption, and high-throughput potential, though challenges remain in terms of equipment costs, resolution for small molecules, and system stability.

Biological methods exploit the inherent chiral recognition of biomolecules such as enzymes, antibodies, and microorganisms, as shown in Fig. 4(b). Enzymatic approaches leverage stereospecific catalysis, converting one enantiomer while leaving the other unreacted, enabling rapid and selective quantification[70]. Target enantiomers can then be separated and quantified by detecting either product signals or residual substrates. For example, glucose oxidase exclusively catalyzes D-glucose to produce hydrogen peroxide, which can be measured via fluorescence imaging. Immunoaffinity chromatography[91] achieves separation using antibodies against a specific chiral configuration. These biological strategies offer mild conditions, environmental compatibility, and high selectivity, but are constrained by enzyme stability, substrate scope, and limited throughput.

In contrast to above non-optical approaches, optical strategies offer several distinctive advantages for chiral sorting. Optical methods enable contactless and non-destructive

manipulation, real-time and in situ control, and flexible programmability through engineered light fields, without the need for chemical derivatization or specific material functionalization. More importantly, optical forces and chiroptical interactions provide access to enantioselective manipulation at the single-particle or even single-molecule level, which is difficult to achieve using conventional chemical or biological routes. These unique features have stimulated growing interest in optical sorting of chiral molecules, which is the primary focus of the following sections.

## 2.2 Optical techniques for chiral sorting

Optical sorting of chiral molecules has evolved along a clear progression in both underlying physical mechanism and optical field complexity. In this section, the discussion is organized starting from fundamental theoretical formulations and advancing toward increasingly sophisticated optical platforms. We first introduce the basic expressions of chiral optical forces derived from light-matter interaction theory, which establish the physical foundation for enantioselective manipulation. Based on these formulations, early demonstrations of optical chiral sorting using relatively simple optical fields, including ORP, OGF, OPF and OLF, are reviewed. Building upon these foundational schemes, the discussion then moves to structured light beams, such as vector beams and tightly focused high-NA fields. Finally, we review near-field and nanophotonic approaches, where strong field confinement and resonant enhancement play a dominant role. Novel platforms including waveguides and metasurfaces are discussed, as they offer orders-of-magnitude enhancement of chiral light-matter interactions and open new routes toward practical, miniaturized, and integrable chiral sorting devices.

**ORP, OGF, OPF and OLF for chiral sorting.** In the next section, we will discuss in detail different optical sorting mechanisms, beginning with some classical works based on the ORP, OGF, OPF, and optical OLF. These formulations provide a unified basis for classifying optical sorting mechanisms according to the physical origin of the chiral force.

The constitutive relation of chiral particles is well established and is given by[20,92]:

$$\begin{cases} \boldsymbol{D} = \varepsilon_{\mathrm{p}}\boldsymbol{E} + \mathrm{i}\kappa\sqrt{\varepsilon_0\mu_0}\boldsymbol{H} \\ \boldsymbol{B} = -\mathrm{i}\kappa\sqrt{\varepsilon_0\mu_0}\boldsymbol{E} + \mu_{\mathrm{p}}\boldsymbol{H} \end{cases}, \tag{1}$$

where $\varepsilon_{\mathrm{p}}$ and $\mu_{\mathrm{p}}$ are permittivity and permeability of the particle, respectively and $\kappa$ is the chirality parameter constrained by $\kappa < \sqrt{\varepsilon\mu}$. Here, $\varepsilon$ and $\mu$ represent the permittivity and permeability of the medium[93,94].

The induced electromagnetic dipole moments in chiral particles are determined by the incident electromagnetic field and the corresponding polarizabilities[38,95–97]:

$$\begin{cases} \boldsymbol{d} = \alpha_{\mathrm{ee}}\boldsymbol{E} + \alpha_{\mathrm{em}}\boldsymbol{B} \\ \boldsymbol{m} = -\alpha_{\mathrm{em}}\boldsymbol{E} + \alpha_{\mathrm{mm}}\boldsymbol{B} \end{cases}, \tag{2}$$

where $\boldsymbol{E}$ and $\boldsymbol{B}$ represent the incident electric and magnetic fields, respectively, $\alpha_{\mathrm{ee}}$, $\alpha_{\mathrm{mm}}$, and $\alpha_{\mathrm{em}}$ are the electric, magnetic, and magnetoelectric polarizabilities of the particles. The polarizability $\alpha_{\mathrm{em}}$ is related to the chirality parameter $\kappa$ of the particles, and varies with the sign of $\kappa$. For achiral particles, $\alpha_{\mathrm{em}} = 0$. The polarizabilities $\alpha_{\mathrm{ee}}$, $\alpha_{\mathrm{mm}}$, and $\alpha_{\mathrm{em}}$ are related to the Mie coefficients $a_1$, $b_1$, and $c_1$.

$$\alpha_{\mathrm{ee}} = \frac{\mathrm{i}6\pi\varepsilon\varepsilon_0}{k^3}a_1,\ \alpha_{\mathrm{mm}} = \frac{\mathrm{i}6\pi\mu\mu_0}{k^3}b_1,\ \alpha_{\mathrm{em}} = \frac{6\pi}{\omega k^2}c_1\ . \tag{3}$$

The scattering coefficients are defined as:

$$\begin{cases} a_n = \dfrac{V_n(\mathrm{R})A_n(\mathrm{L}) + V_n(\mathrm{L})A_n(\mathrm{R})}{W_n(\mathrm{L})V_n(\mathrm{R}) + W_n(\mathrm{R})V_n(\mathrm{L})} \\ b_n = \dfrac{W_n(\mathrm{L})B_n(R) + W_n(\mathrm{R})B_n(\mathrm{L})}{W_n(\mathrm{L})V_n(\mathrm{R}) + W_n(\mathrm{R})V_n(\mathrm{L})} \\ c_n = \mathrm{i}\dfrac{W_n(\mathrm{R})A_n(\mathrm{L}) - W_n(\mathrm{L})A_n(\mathrm{R})}{W_n(\mathrm{L})V_n(\mathrm{R}) + W_n(\mathrm{R})V_n(\mathrm{L})} \end{cases}, \tag{4}$$

with

$$\begin{cases} W_n(J) = m\psi_n(m_J X)\,\xi_n'(X) - \xi_n(X)\psi_n'(m_J X) \\ V_n(J) = \psi_n(m_J X)\,\xi_n'(X) - m\xi_n(X)\psi_n'(m_J X) \\ A_n(J) = m\psi_n(m_J X)\,\psi_n'(X) - \psi_n(X)\psi_n'(m_J X) \\ B_n(J) = \psi_n(m_J X)\,\psi_n'(X) - m\psi_n(X)\,\psi_n'(m_J X) \end{cases}, \tag{5}$$

here, $X = ka$, with $a$ representing the particle's radius and $J = \mathrm{L}, \mathrm{R}$ stands for left and right chirality, respectively; $\psi_n(\rho) = \rho j_n(\rho)$, $\xi_n(\rho) = \rho h_n^{(1)}(\rho)$, $j_n(\rho)$ and $h_n^{(1)}(\rho)$ denote the spherical Bessel function and the first kind of spherical Hankel function. The relative refractive indices $m_{\mathrm{L}}$, $m_{\mathrm{R}}$ and the averaged refractive index $m$ can be expressed as $m_{\mathrm{L}} = \sqrt{\varepsilon_{\mathrm{p}}\mu_{\mathrm{p}}/\varepsilon\mu} + \kappa$, $m_{\mathrm{R}} = \sqrt{\varepsilon_{\mathrm{p}}\mu_{\mathrm{p}}/\varepsilon\mu} - \kappa$, and $m = (m_{\mathrm{L}} + m_{\mathrm{R}})/2$, respectively.

The time-averaged optical force exerted by an electromagnetic field $\boldsymbol{E}$ and $\boldsymbol{B}$ on a dipolar particle is given by[94,98,99]:

$$\boldsymbol{F} = \frac{1}{2}\mathrm{Re}\left[\boldsymbol{d}\cdot(\nabla)\boldsymbol{E}^* + \boldsymbol{m}\cdot(\nabla)\boldsymbol{B}^* - \frac{k^4}{6\pi\varepsilon c}(\boldsymbol{d}\times\boldsymbol{m}^*)\right]\ . \tag{6}$$

Then, the expression for the optical force on chiral particles can be derived as follows[95,100]:

$$\begin{aligned} \langle\boldsymbol{F}\rangle =& \boldsymbol{F}_{\mathrm{grad}} + \boldsymbol{F}_{\mathrm{rad}} + \boldsymbol{F}_{\mathrm{curl}} + \boldsymbol{F}_{\mathrm{vor}} + \boldsymbol{F}_{\mathrm{spin}} + \boldsymbol{F}_{\mathrm{flow}} \\ =& -\nabla\langle U\rangle + \frac{1}{c}(C_{\mathrm{ext}} + C_{\mathrm{recoil}})\langle\boldsymbol{P}\rangle + C_{\mathrm{p}}c\nabla\times\langle\boldsymbol{S}_{\mathrm{e}}\rangle \\ &+ C_{\mathrm{m}}c\nabla\times\langle\boldsymbol{S}_{\mathrm{m}}\rangle + \mu\mathrm{Re}(\alpha_{\mathrm{em}})\nabla\times\langle\boldsymbol{P}\rangle \\ &+ \left[\gamma_{\mathrm{e}}\langle\boldsymbol{S}_{\mathrm{e}}\rangle + \gamma_{\mathrm{m}}\langle\boldsymbol{S}_{\mathrm{m}}\rangle\right] + \frac{ck^4\mu^2}{12\pi}\mathrm{Im}(\alpha_{\mathrm{em}}\alpha_{\mathrm{mm}}^*)\mathrm{Im}(\boldsymbol{E}\times\boldsymbol{H}^*)\ . \end{aligned} \tag{7}$$

From Eq. (7), the optical force on chiral particles can be categorized into six components based on their origins. Here, $\boldsymbol{F}_{\mathrm{grad}}$ denotes the OGF, with its potential given by $\langle U\rangle = -\frac{1}{4}\mathrm{Re}(\alpha_{\mathrm{ee}})|\boldsymbol{E}|^2 - \frac{1}{4}\mathrm{Re}(\alpha_{\mathrm{mm}})|\boldsymbol{H}|^2 - \frac{1}{2}\mathrm{Re}(\alpha_{\mathrm{em}})\,\mathrm{Im}(\boldsymbol{E}\cdot\boldsymbol{B}^*)$; $\boldsymbol{F}_{\mathrm{rad}}$ is the ORP, proportional to the time-averaged Poynting

vector $\langle \boldsymbol{P} \rangle$. The cross-section $C_{\rm ext} = C_{\rm p} + C_{\rm m}$ is a summation of the electric- and magnetic-dipole part, written as $C_{\rm p} = k{\rm Im}(\alpha_{\rm ee})/\varepsilon$ and $C_{\rm m} = k\mu{\rm Im}(\alpha_{\rm mm})$. The term $C_{\rm recoil} = -\dfrac{k^4\mu}{6\pi\varepsilon}\left[{\rm Re}\left(\alpha_{\rm ee}\alpha_{\rm mm}^*\right) + |\alpha_{\rm em}|^2\right]$ is the cross-section directly associated with the recoil force[101]; the force $\boldsymbol{F}_{\rm curl}$ originate from $\nabla \times \langle \boldsymbol{S} \rangle$ ($\boldsymbol{S}$ is the spin angular momentum (SAM)) while the force $\boldsymbol{F}_{\rm vor}$ originates from $\nabla \times \langle \boldsymbol{P} \rangle$ which is also known relevant to optical torques on achiral particles[102–104]; $\boldsymbol{F}_{\rm spin}$ results from the contributions of $\boldsymbol{S}_{\rm e}$, and $\boldsymbol{S}_{\rm m}$, where $\boldsymbol{S}_{\rm e}$, and $\boldsymbol{S}_{\rm m}$ representing the electric and magnetic SAM, respectively. $\gamma_{\rm e} = 2\omega^2\mu{\rm Re}\left(\alpha_{\rm em}\right) - \dfrac{k^5}{3\pi\varepsilon^2}{\rm Im}\left(\alpha_{\rm ee}\alpha_{\rm em}^*\right)$ and $\gamma_{\rm m} = 2\omega^2\mu{\rm Re}\left(\alpha_{\rm em}\right) - \dfrac{k^3\mu}{3\pi\varepsilon}{\rm Im}\left(\alpha_{\rm mm}\alpha_{\rm em}^*\right)$; $\boldsymbol{F}_{\rm flow}$ is associated with the imaginary component of the Poynting vector, which is widely studied recently[105,106]. Together, these forces describe fundamental mechanisms of optical sorting for chiral particles, and form the basis for subsequent developments in enantioselective manipulation using light.

Light carries both linear and angular momentum, which can be transferred to particles, enabling light-matter interactions and underpinning a wide range of optical manipulation strategies. ORP, the mechanical effect of linear momentum transfer from light to matter, occurs when light is refracted, reflected, scattered, or absorbed. This phenomenon is prominently applied in atomic cooling[107–109], optical sorting, particle propulsion, and related areas. Chiral particles of opposite handedness experience distinct ORPs under illumination with circularly polarized light of opposite helicity[36]. After the conceptual proposal of optical sorting using the ORP in 2013[36], two teams from Brasselet's and Cipparrone's groups conducted experiments in 2014[110,111]. Using two counter-propagating beams with opposite helicity, left- and right-handed chiral particles can be pushed to the right and left sides, respectively, resulting in the efficient sorting, as shown in Fig. 5(a). Abujetas et al. investigated the transverse spin in the guided mode, which can exert the ORP on chiral particles and enable efficient sorting[112].

The OGF is another efficient force correlated strongly to the chirality parameter[113] arising from the inhomogeneous intensity of the optical field and is directed along the gradient of light intensity. This force either attracts particles toward regions of higher intensity or repels them from such regions. The OGF is fundamental in optical tweezers, which have a wide range of applications, including optical trapping[114], bioprospecting, particle sorting, biomolecule stretching, and the study of interactions between biological entities. Specifically, the chiral OGF refers to the component of the gradient force that is influenced by the chirality of the particles. Unlike conventional OGF components,

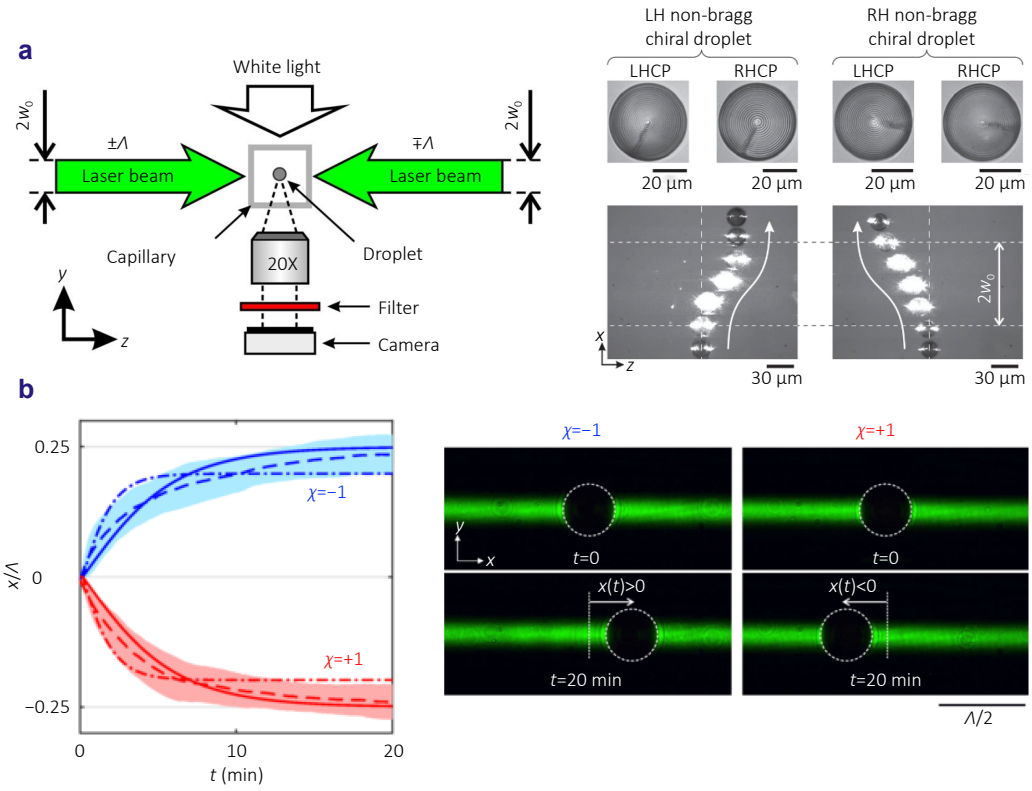



Fig. 5 | Optical radiation pressures and optical gradient forces for chiral sorting. (a) ORP using counter-propagating beams of opposite helicity, enabling opposite enantiomers to move in opposite directions. (b) Helicity-dependent displacement of particles arising from OGF, which is strongly correlated with the chiral polarizability of the analytes. Figure reproduced with permission from: (a) ref.[110], Springer Nature; (b) ref.[39], American Physical Society.

which depend on the intensity inhomogeneity of the incident light field, the chiral OGF can be generated even in an optical field with uniform light intensity[115]. Chiral particles can be selectively trapped or repelled from a tightly focused trap, which is principally feasible for chiral sorting[37,111,116–120]. Helicity gradient serves as another interesting toolkit for sorting chiral particles. For instance, Kravets et al. reported the selective displacement of chiral particles with different handedness in a line-shaped light field with helicity gradient[39], as shown in Fig. 5(b). Though physically interesting, this type of optical force is exceedingly small, at least two orders of magnitude smaller than the conventional optical gradient force.

Recently, the OLF has been utilized for chiral sorting. The OLF, a unique force acting perpendicular to the direction of light propagation and independent of both intensity and phase gradients, has garnered significant attention due to its intriguing underlying physics and potential applications in enantiomer sorting. The generation of an OLF relies on breaking the symmetry of the system, allowing light to transfer lateral momentum to an object. Various mechanisms can produce OLFs, including the coupling of light with the object's chirality[121,122], spin-orbit interaction[123–125], and surface plasmon polaritons (SPPs)[126–128]. The generation of an OLF relies on breaking the symmetry of the system, allowing light to transfer lateral momentum to an object. In a plane wave, Wang and Chan proposed the fundamental mechanism of the leverage of the OLF for sorting chiral particles with opposite handedness[38]. The experimental demonstration has been hugely lagging behind. In 2021, Shi et al. placed chiral particles at the interface of air and water and illuminated them with a linearly polarized light wave, as shown in Fig. 6(a)[92]. Through the transverse transfer of momentum of light and particle, an OLF is generated to separate chiral particles. A simple plane wave requires the assistance of the interface for chiral sorting. A constructive beam, such as standing waves from two wave interference can generate OLFs directly. Chen et al. achieved the chiral sorting using a standing wave from two linearly polarized beams[95], as shown in Fig. 6(b). The mechanism relies on the generation of transverse spin, as shown in Eq. (7). The standing wave can also be configured from two waves with different polarizations[96], such as linearly and elliptically polarized light beam (Fig. 6(c)). In this case, multiple forces can coordinate, such as forces from the transverse spin and spin momentum, making this method more efficient and dynamic than the linear case in Fig. 6(b). Recently, Shi et al. observed the intricate chiral optical force on a chiral sphere in a spin-curl light field, as shown in Fig. 6(d)[129]. A chiral particle is placed on a surface and illuminated with an elliptically polarized focused beam. In this system, multiple parameters, such as the transverse spin, Belinfante spin momentum and energy vortex (curl of the energy flow), all could have profound effects on the chiral OLF. In their work, they have achieved sorting of chiral particles with different sizes and handedness. By switching different polarizations of light, the direction of OLF on the chiral particles can be switched.

Apart from the intriguing OLF, the counterintuitive OPF can also be employed for chiral sorting. Previous studies have successfully demonstrated optical manipulation techniques, such as pushing, trapping, and rotating tiny objects ranging from nanometers to tens of micrometers in size. However, manipulating objects through backward pulling has remained elusive and counterintuitive. Generally, with a standard beam lacking a longitudinal gradient, it is expected that an object illuminated by light would be pushed forward. Yet, about a decade ago, researchers discovered a new and counterintuitive phenomenon known as the OPF, which pulls an object toward the light source[101,130–132]. Ali et al. used two circularly polarized beam to construct an interference field and control the incident angle for selectively generate an OPF on a specific chiral particle[41], as shown in Fig. 6(e). When the number of light beams becomes three, an OPF can also be generated (Fig. 6(f))[133]. Zheng et al. designed an interferential optical field which is composed of three plane waves with the same circular polarization, to sort chiral particles, which obviously improves the experimental feasibility attributing to the relatively wide tunable range of the directions of wave vectors. In this system, particles with certain chirality will be stably trapped in the periodic intensity maximum spot, exerted by an optical pulling force along the $-z$ direction.

**Structured light beams for chiral sorting.** The force magnitude and spatial selectivity achievable with simple optical fields remain limited. We then focus on the discussion of the structured light beams with additional degrees of freedom for chiral force engineering. A typical example is the vector beam. Li et al. reported a fundamental scheme to selectively trap and repel chiral particles with opposite real parts of the chirality parameter[42]. By controlling the imaginary parts of the chirality parameter, different particles can rotate clockwise or counter-clockwise in the vector beam. Later, the same team utilized a focused vector beam with orbital angular momentum for particle manipulation[134,135], as shown in Fig. 7(a). Focused vector vortex beams carrying radial-splitting optical chirality can electively trap one chiral particle inside or outside the intensity maxima depending on the sign of the orbital angular momentum. Chiral particles with different handedness can be trapped on different orbits and experience enhanced optical forces. Vector beams carrying different topological charges transfer angular momentum to chiral particles with opposite handedness differently, resulting in an enantioselective optical force to either push or repel certain chiral particles[136].

As shown in Fig. 7(b), Xiong et al. proposed an optical method that selectively traps enantiomers by using tightly focused fractional vector beams[137]. In their proposed model, such a focused beam forms multiple local optical CDs with opposite signs at the focal plane. They found that focused

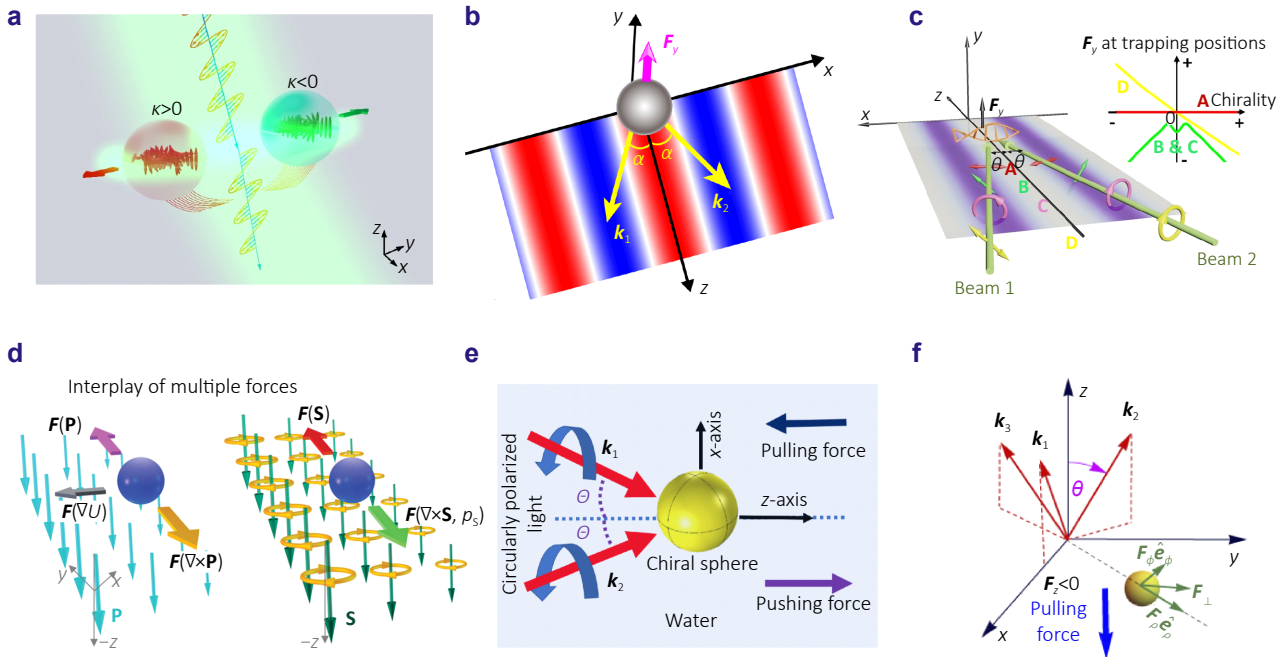



Fig. 6 | Optical lateral forces and optical pulling forces on chiral particles. (a) Separating chiral particles placed at the interface of air and water with a linearly polarized light wave. (b) Chiral sorting using a standing wave from two linearly polarized beams. (c) OLF on chiral particles resulted from a standing wave configured from two waves with different polarizations. (d) Observation of multiple-parameter chiral optical force on a chiral sphere in a spin-curl light field. (e) Chiral sorting by OPF generated from an interferential field constructed of two circularly polarized beams. (f) Chiral sorting by OPF generated from an interferential field composed of three circularly polarized beams. Figure reproduced with permission from: (a) ref.[92], 2020 Springer Nature; (b) ref.[95], American Physical Society; (c) ref.[96], American Chemical Society; (d) ref.[129], American Physical Society; (e) ref.[41], Optica Publishing Group; (f) ref.[133], Optica Publishing Group.

fractional vector beams can stably trap the enantiomers at the local positions with the minimum or maximum CDs according to the handedness of enantiomers. Their work may find applications in achieving precise and stable capture of multiple pairs of enantiomers.

In addition to these methods, Li et al. designed a controllable chiral optical field by tightly focusing two tailored vector beams in a 4π optical microscopic system with two high-NA objective lenses, as shown in Fig. 7(c)[138]. By modulating the wavefronts of the incident vector beams with appropriately designed phase masks, a chiral optical field with multiple spots carrying switchable handedness or controllable chirality can be generated. The location, the number and the handedness of such chiral spots can be arbitrarily adjusted depending on the actual application requirements. This controllable chiral field has practical application value for achieving precise and stable enantioselective separation, chiral detection and chiral sensing at the nanoscale.

Recently, Li et al. developed a novel optical method for chiral enantiomer sorting by inversely designing the polarization state of an input Gaussian beam focused through a high-NA objective lens (Fig. 7(d))[139]. The technique employs orthogonal circular polarization bases with a spatially varying phase to generate tailored chiral optical fields. This creates twin foci with opposite optical chirality densities in the focal plane, enabling simultaneous trapping of left- and right-handed enantiomers at predetermined positions. The approach achieves non-contact separation of chiral particles with freely adjustable trapping positions, offering significant value for pharmaceutical research and chiral sensing applications.

Other attempts include the utilization of structured caustic vector vortex field[140], multiple longitudinal polarization vortex structures[141], focused vector polarized hollow beams[142], coordination of two vector beams[138], vector Lissajous beams[143], etc.

**Near-field and nanophotonic for chiral sorting.** Free-space methods normally generate relatively small optical forces due to loosely confined light fields. A further leap in force enhancement requires the subwavelength field confinement, naturally leading to near-field and nanophotonic platforms. Near-field configures with a diversity of mechanisms show promising in enhancing optical forces and enabling efficient chiral sorting[144]. The chiral polarizability and optical force in the near field are much greater than the far field[113]. Typical examples include evanescent waves, optical fibers and waveguides. Shortly after the introduction of the OLF in 2014, Hayat et al. excited the transverse spin in an evanescent wave via the total internal reflec-

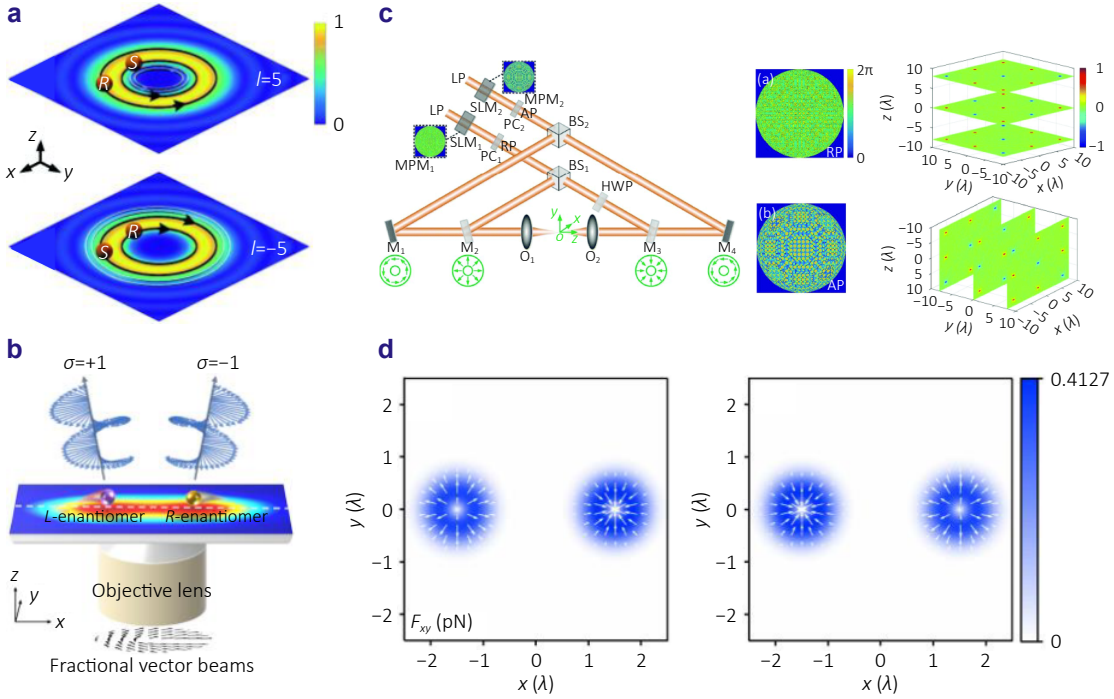



Fig. 7 | Structure light beams for enantioselective optical manipulation. (a) The optical separation and discrimination of chiral particles using the focused vector vortex beam carrying the orbital angular momentum. (b) Trapping chiral particles using tightly focused FVBs. (c) The 4π microscopic system integrated with MPMs encoded by phase-only SLMs for achieving a controllable chiral optical field. (d) Chirality-sorting optical force pairs generated in a tightly focused Gaussian beam by tailoring the input polarization state. Figure reproduced with permission from: (a) ref.[134], under a Creative Commons Attribution-Non Commercial 3.0 Unported Licence; (b) ref.[137], Optica Publishing Group; (c) ref.[138], Royal Society of Chemistry; (d) ref.[139], American Physical Society.

tion in 2015[145]. Linearly polarized light generates the transverse spin perpendicular to the incident plane and generate the OLF, as shown in Fig. 8(a). This force is demonstrated to be greater than that generated by placing the chiral particle on a surface and illuminating it using a linearly polarized plane wave[38]. Cao et al. proposed a graphene-coated chalcogenide nanowire to produce mid-infrared, chiral surface plasmon polaritons, which can be switched on and off by non-volatile structural state transitions in the dielectric constants of the chalcogenide glass. Chiral particles with size of sub-10 nm and having opposite handedness experience OLFs that differ in magnitude and sign, resulting efficient chiral sorting[146], as shown in Fig. 8(b).

Compared with reconfigurable nanowires, waveguides are more common with standard fabrication process. Fang et al. reported an intriguing chiral sorting configuration using the slot waveguide[43], as shown in Fig. 8(c). The counter-propagating slot waveguides generate strongly enhanced electromagnetic chirality gradient that is confined in the slot. Chiral particles with opposite handedness can be trapped in two potential wells in different positions, paving the way for large-scale chiral sorting in optofluidic systems. Martínez-Romeu et al. systematically investigated the chiral optical forces on dielectric waveguides for chiral sorting[147], as shown in Fig. 8(d). Chiral optical forces under the quasi-TE modes at 405 nm and combined effect from the quasi-TE and quasi-TM modes at 1310 nm, demonstrating the efficient separation of chiral nanoparticles in two seconds. This method shows that the SiN waveguides have a great efficiency in chiral sorting, greatly reducing the consumed sorting time.

Recently, optical sorting using metasurfaces has raised a great diversity of attention in the past few years[148]. Those methods leverage the strong capabilities of metasurfaces in manipulating the intensity, phase and polarization distributions of light and versatile near-field manipulation configurations. Metasurfaces have been utilized to sort achiral particles with sizes down to 10 nm[149,150]. They have also shown great efficiency in sorting chiral particles. This particular research direction starts when Solomon et al. utilized the high-index pillar array to enhance the optical chirality[53], which also paves the way for the high-precision detection of chiral molecules.

Cao et al. proposed the Fano-enhanced chiral optical force with visible light using a plasmonic nanoaperture[151], as shown in Fig. 9(a). Multipolar interference Fano resonances are excited under circularly polarized light illumination by the modal energy splitting resulting from the interaction between resonant modes in symmetric outer and asymmetric inner Au split-rings. The lateral chiral and non-chiral gradient forces enable helicity-dependent transverse deflection of chiral nanoparticles above the aperture. This mechanism

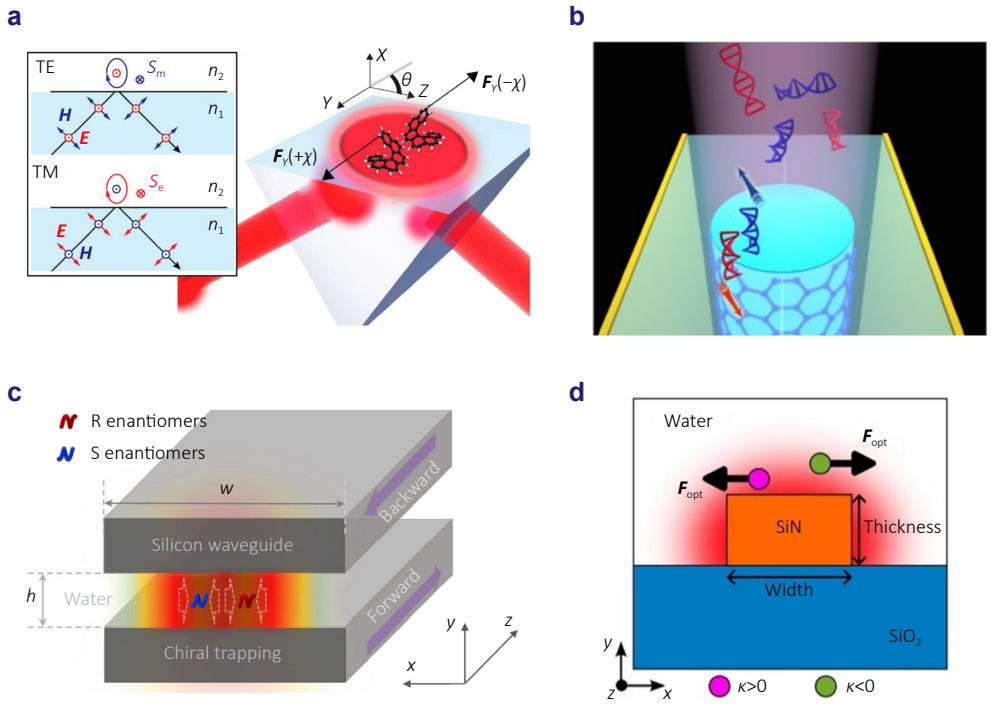



Fig. 8 | Near-field optical configurations for enhanced chiral sorting. (a) Evanescent-wave induced OLF generated by total internal reflection. (b) Graphene-coated nanowires supporting switchable chiral plasmon polaritons. (c) Slot waveguides with strongly confined chirality gradients lending to spatial separation of enantiomers. (d) SiN waveguides exploiting hybrid TE/TM modes for rapid and efficient nanoparticle separation within several seconds. Figure reproduced with permission from: (a) ref.[145], National Academy of Sciences; (b) ref.[146], Springer Nature; (c) ref.[43], American Physical Society; (d) ref.[147], Optica Publishing Group.

offers a promising platform for all-optical efficient chiral sorting. Later, Cao et al. also reported another configuration for the generation the combined dipole-octupole Fano resonance for chiral sorting[152], as shown in Fig. 9(b). Such Fano resonance significantly enhances the chiral gradient force, being capable for sorting sub-10 nm chiral nanoparticles with distinct potential wells. Those approaches sort chiral particles in a static environment, which results in a relatively low throughput. Recently, Zhang et al. reported an architecture with metasurface on top of a multi-layer thin film[45], as shown in Fig. 9(c). This metasurface excites a toroidal dipole mode, which generates enhanced optical forces on sub-20 nm chiral particles. Chiral particles with opposite handedness have potential wells in different locations. They can be sorted in a fast flow velocity of 800 μm/s under the synergy of optical and fluidic forces. This is the first demonstration of sorting chiral particles in a fast flow stream, opening the gate for practical biochemical applications.

There have been quite a few other examples of metasurface-enabled chiral sorting. For instance, Safkat et al. presented a novel all-optical technique for distinguishing classes of nanoscale Mie objects by placing them over a metasurface of double-lined gold nanostructures. This configuration enables efficient on-chip sorting of silica (dielectric), gold (plasmonic), and chiral nanospheres[153]. Tang et al. proposed an on-chip platform using surface plasmon polaritons to generate five transformable topological optical lattices via tunable polarization and phase vortices, overcoming limitations of traditional complex systems[154]. Through dipolar analysis and simulations, they show that the spin density force is the key mechanism for out-of-plane sorting of large chiral particles (radius > 100 nm) and introduce a dual-function microflow system for trapping and sorting.

Notably, recent years have witnessed the fast development of fascinating new physics using metasurfaces. Well-known examples are BICs[155–163] and EPs[28,164–172]. Recently, Mao et al. presented a silicon metasurface featuring nanodisks with offset holes, which supports a sharp quasi-BIC (qBIC) magnetic dipolar resonance originating from symmetry breaking. This qBIC MD resonance significantly enhances the chiral lateral force on sub-2 nm enantiomers under linear polarization by generating a strong chirality density gradient with alternating sign around the disk, while exhibiting minimal electromagnetic density gradient[44], as shown in Fig. 10(a). It also creates four pairs of deep optical potential wells ($\sim$13 $k_BT$) uniformly distributed around the resonator edge, enabling simultaneous separation of four enantiomer pairs, thereby advancing all-optical enantioseparation. Based on similar principles, left-handed and right-handed nanoparticles could experience distinct potential

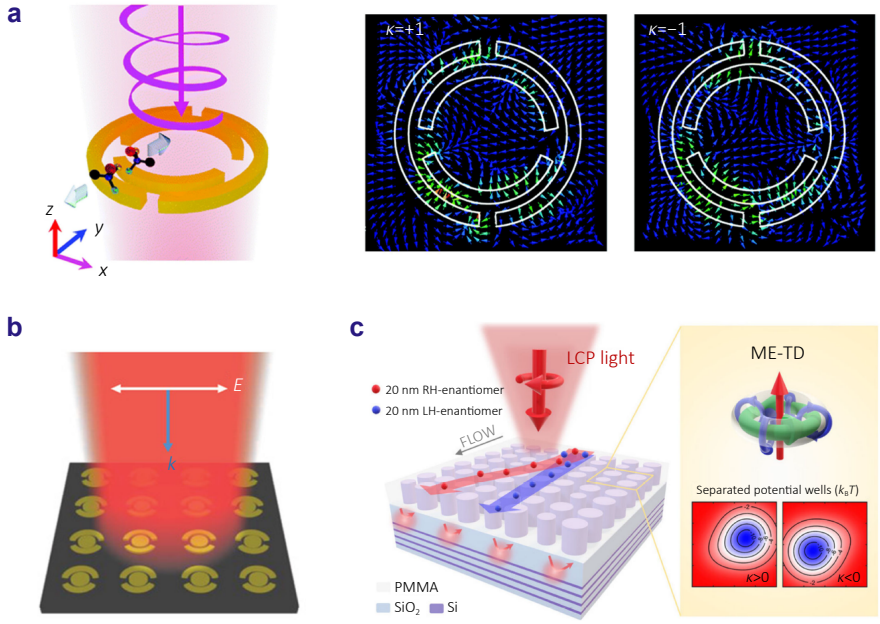



Fig. 9 | Metasurface-assisted chiral sorting via multipolar interference. (a) Plasmonic split-ring apertures enabling Fano-enhanced chiral forces. (b) Dipole-octupole Fano resonances generating strong enantioselective for sorting sub-10 nm particles. (c) Toroidal dipole metasurface producing enhanced forces in flowing liquid streams, demonstrating high-throughput enantioseparation. Figure reproduced with permission from: (a) ref.[151], Royal Society of Chemistry; (b) ref.[152], Wiley-VCH GmbH; (c) ref.[45], American Chemical Society.

wells with different positions or depths using BICs[173,174].

Recently, Jin et al. designed metasurfaces based on asymmetric silicon dimers supporting dual qBICs[175] (Fig. 10(b)). These qBICs were engineered to achieve near-perfect spatial overlap of electric and magnetic fields near their anti-crossing point, resulting in a remarkable $10^4$-fold enhancement of the superchiral field. Enantioselective optical forces on single molecules reaching magnitudes of pN/mW·μm$^2$ were thus generated. Furthermore, switching of the superchiral field's handedness and the resulting force direction was enabled by encircling the anti-crossing point. Analysis of the qBIC-assisted chiral separation dynamics highlights the promising potential of this approach for applications in chiral sensing and sorting with profound precision.

An exceptional point is a special type of degeneracy occurring in non-Hermitian systems (like those with loss or gain) where not only eigenvalues (frequencies) but also the corresponding eigenvectors (modes) of the system coalesce. A two-mode non-Hermitian system can be described by the Hamiltonian:

$$\boldsymbol{H}=\begin{bmatrix}\omega_1-\mathrm{i}\gamma_1 & \kappa\\ \kappa & \omega_2-\mathrm{i}\gamma_2\end{bmatrix}, \tag{8}$$

where $\omega_{1,2}$ and $\gamma_{1,2}$ denote the resonance frequencies and the gain/loss rate of the two modes, respectively, and $\kappa$ is the coupling strength. The eigenvalues are obtained as:

$$E=\omega_{\mathrm{ave}}-\mathrm{i}\gamma_{\mathrm{ave}}\pm\sqrt{\left(\omega_{\mathrm{diff}}-\mathrm{i}\gamma_{\mathrm{diff}}\right)^2+\kappa^2}, \tag{9}$$

where $\omega_{\mathrm{ave}}=(\omega_1+\omega_2)/2$, $\gamma_{\mathrm{ave}}=(\gamma_1+\gamma_2)/2$, $\omega_{\mathrm{diff}}=(\omega_1-\omega_2)/2$, and $\gamma_{\mathrm{diff}}=(\gamma_1-\gamma_2)/2$. For a PT-symmetric system, where $\omega_1=\omega_2=\omega_0$ and $\gamma_1=-\gamma_2=\gamma_0$, the eigenvalues simplify to $E=\omega_0\pm\sqrt{\kappa^2-\gamma_0^2}$. Here, the system exhibits a phase transition: when $\kappa>\gamma_0$, the eigenvalues remain real (unbroken PT phase), while for $\kappa<\gamma_0$, they form complex-conjugate pairs (broken PT phase). At the critical condition $\kappa=\gamma_0$, the two eigenvalues and eigenvectors simultaneously merge, giving rise to an EP. This coalescence leads to unique properties, such as extreme sensitivity to perturbations and topological features, making EPs valuable for designing sensors, lasers, and devices controlling light in novel ways[176,177]. Though interesting, this topic only has a few works at present. Zhang et al. demonstrated enhanced optical forces on chiral particles positioned within a non-Hermitian waveguide lattice[178], achieving EPs through unidirectional coupling under linear plane wave excitation, as confirmed by full-wave simulations. Furthermore, they found that higher-order EPs generally yield stronger forces, which exhibit a distinct skin effect, maximizing at one end of the particle lattice. Recently, Liu designed a silicon microfluidic chip leveraging a vector EP, formed by breaking mirror-symmetry in lossy waveguides to couple orthogonal modes, to achieve highly efficient chiral nanoparticle separation[179], as shown in Fig. 10(c). This vector EP generates a powerful superchiral gradient field within the chip, inducing strong chiral gradient forces that drive nanoparticles of opposite handedness to opposite sides of an extended slot. Furthermore, cascaded vector EPs in a single chip are implemented to significantly increase the spatial separation distance,

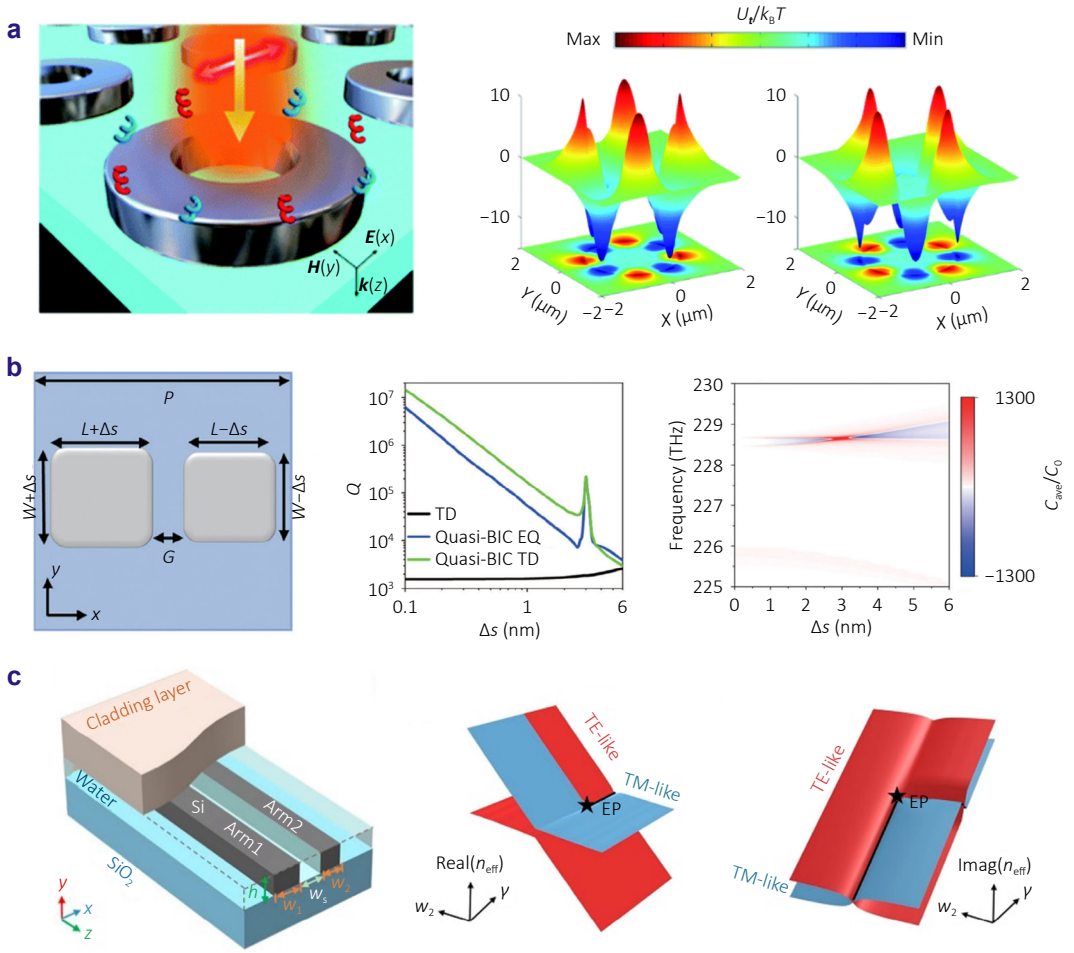



Fig. 10 | Novel metasurface physics for chiral sorting. (a) qBIC magnetic dipole resonance producing strong chirality density gradients for sub-2 nm particle separation. (b) Dual qBIC silicon dimers achieving near-perfect field overlap and $10^4$-fold superchiral enhancement. (c) Vector exceptional point metasurface integrated with microfluidics, generating powerful chiral gradient forces for efficient on-chip enantioseparation. Figure reproduced with permission from: (a) ref.[44], Royal Society of Chemistry; (b) ref.[175], American Physical Society; (c) ref.[179], under a Creative Commons Attribution (CC BY) license.

demonstrating the feasibility and efficiency of this approach through particle tracking simulations accounting for nanoparticle thermal motion.

Beyond optomechanical interactions, it is worth noting that chiral separation can also be achieved using other physical field-based approaches, such as electric[180], magnetic[181], and acoustic[182] fields. For example, chiral particles placed in rotating electric fields may experience enantioselective transport, resulting in opposite motion depending on their handedness. Similarly, enantiospecific interactions have been demonstrated for chiral molecules coupled to perpendicularly magnetized substrates. While these approaches offer valuable complementary pathways for chiral separation, they typically depend on material-specific responses, complex device configurations, or additional operation steps. In contrast, optical sorting enables contactless, non-destructive, and highly tunable manipulation through engineered light-matter interactions, allowing chiral selectivity to be flexibly programmed using optical fields alone.

## 3 Chiral detection

In this section, we first briefly review representative non-optical methods for chiral detection, and then systematically survey optical approaches, with an emphasis on recent advances in chiral detection enabled by enhanced superchiral electromagnetic fields.

### 3.1 Non-optical techniques for chiral detection

For non-optical detections, electrochemical methods are particularly powerful, where chiral discrimination is achieved by modifying electrodes with chiral selectors (e.g., cyclodextrins, amino acids, quinidine derivatives, or chiral polymers) or employing chiral ionic liquids. Enantiomers exhibit different redox potentials or electron transfer kinetics at these chiral interfaces, allowing their differentiation via voltammetric techniques like cyclic voltammetry or differential pulse voltammetry. The mass spectrometry coupled with

chiral separation techniques like chromatography or electrophoresis provides another potent non-optical route. While the mass spectrometry itself is not inherently chiral, it becomes a chiral detector when paired with methods that separate enantiomers before ionization, or by using chiral matrices or ion-mobility separation that can exploit subtle differences in ion-mobility cross-sections or fragmentation patterns between enantiomers. Other non-optical strategies leverage the principles of separation science and specific interactions at chiral interfaces. High-performance liquid chromatography and gas chromatography equipped with CSPs remain workhorses for chiral analysis and preparative separation. These CSPs, composed of materials like derivatized cyclodextrins, macrocyclic glycopeptides (e.g., vancomycin), or Pirkle-type phases, selectively retain one enantiomer over the other based on diastereomeric complex formation, enabling detection via universal detectors like refractive index or evaporative light scattering, avoiding the need for chromophores. Nuclear Magnetic Resonance (NMR) spectroscopy, while technically involving electromagnetic radiation, detects chirality through chemical shifts rather than optical activity; chiral solvating agents or chiral shift reagents form transient diastereomeric complexes with enantiomers, causing their NMR signals to split, allowing quantification. Additionally, sensor technologies like quartz crystal microbalances or field-effect transistors functionalized with chiral recognition elements can transduce the selective binding of one enantiomer into measurable electrical or mass signals. These diverse non-optical approaches provide crucial tools for chiral analysis, especially for molecules lacking strong chromophores or when high-throughput analysis is required. For more detailed overview of chiral detection using non-optical methods, one can refer to abundant review papers[70,183–191]. While non-optical techniques provide mature and accurate chiral detection, they typically rely on chemical or separation-based processes, normally lack real-time and in-situ capabilities, and largely limited to ensemble-averaged measurements. In contrast, optical approaches enable contactless, non-destructive, and real-time detection with minimal sample preparation, and recent nanophotonic and superchiral field engineering have made them particular powerful for detecting weak chiral signals.

### 3.2 Optical techniques for chiral detection

Prior to 2020, the detection and structural characterization of chiral molecules relied heavily on advanced spectroscopic techniques exploiting their intrinsic chiroptical responses. CD spectroscopy stands as the gold standard, directly probing the differential absorption of left- and right-circularly polarized light. This provides unparalleled insights into the absolute configuration of small molecules, conformational dynamics, and the secondary structure of critical biomolecules like proteins and nucleic acids, cementing its role as an indispensable tool across chemistry, biochemistry, and pharmaceutical research. Optical rotatory dispersion[18,192,193] (ORD) measures how much a chiral molecule rotates the plane of linearly polarized light, and how this rotation changes with the light's wavelength (or colour). Although CD spectroscopy largely replaced ORD for routine quantitative analysis, ORD still provides valuable insights that complement CD data. It is also historically one of the major techniques for studying chirality with light. Furthermore, ORD remains essential for applying specific rules (like the octant rule) that connect spectral patterns to molecular structure, and for fundamental research in chiroptical phenomena. Both techniques primarily operate in the ultraviolet-visible range, requiring suitable chromophores. Significantly, by 2020, vibrational counterparts had matured into powerful, complementary methodologies: Vibrational Circular Dichroism[193,194] (VCD) measured analogous differential absorption in the infrared region, arising from vibrational transitions. This provided atomic-level resolution of stereochemistry and conformation, uniquely enabling the analysis of molecules lacking UV-Vis chromophores. Raman Optical Activity[195], detecting the differential scattering intensity of right- versus left-circularly polarized light, emerged as a particularly robust probe for biomolecular structure in aqueous environments, delivering rich information on dynamic conformational ensembles. Photoelectron circular dichroism[196,197] (PECD) represents another powerful and well-established technique for chiral detection, particularly in the gas phase. Unlike conventional optical circular dichroism, PECD arises from the forward-backward asymmetry in the angular distribution of photoelectrons emitted from chiral molecules under circularly polarized light, leading to significantly enhanced chiral sensitivity. Importantly, PECD does not rely on magnetic dipole transitions and can yield asymmetries of several percent even for randomly oriented molecules, making it an important complementary technique for probing molecular chirality.

Superchiral light refers to an electromagnetic field whose local optical chirality density significantly exceeds that of circularly polarized plane waves. These plane waves are the standard source of chirality in traditional techniques like CD. The mathematical formulation of optical chirality can be traced back to 1964 by Lipkin[198] in the context of electromagnetic conservation laws. However, this quantity was long regarded as mathematically elegant but physically insignificant. Optical chirality $C$ is formally defined as:

$$C = \frac{\varepsilon_0}{2}\boldsymbol{E}\cdot\nabla\times\boldsymbol{E} + \frac{1}{2\mu_0}\boldsymbol{B}\cdot\nabla\times\boldsymbol{B}\,, \tag{10}$$

which can be simplified to the more widely adopted form[199]:

$$C = -\frac{\omega}{2c^2}\mathrm{Im}\left(\boldsymbol{E}^*\cdot\boldsymbol{H}\right) = -\frac{\omega}{2c^2}\left|\boldsymbol{E}\right|\left|\boldsymbol{H}\right|\cos\left(\beta_{\boldsymbol{E},\boldsymbol{H}}\right)\,, \tag{11}$$

where $\varepsilon_0$ and $\mu_0$ are the permittivity and permeability of free

space, $\omega$ is the angular frequency, $c$ is the speed of light, and $\boldsymbol{E}$, $\boldsymbol{B}$, $\boldsymbol{H}$ denote the complex electric, magnetic and auxiliary magnetic field vectors, respectively. The term $\beta_{i\boldsymbol{E},\boldsymbol{H}}$ denotes the phase angle between i$\boldsymbol{E}$ and $\boldsymbol{H}$. This quantity effectively characterizes both the handedness and the strength of chirality in an electromagnetic field. Therefore, maximizing optical chirality requires simultaneously satisfying three key conditions for electric and magnetic field components: (i) strong and spectrally overlapping amplitudes, (ii) parallel and spatially coincident field distributions, and (iii) a phase difference of π/2 between them.

The physical relevance of optical chirality was revitalized in 2010[200], when Tang et al. first proposed the concepts of "superchiral light" and "optical chirality". They demonstrated that the absorption rate of chiral molecules is governed not only by their intrinsic chiral polarizabilities but also by the optical chirality of the surrounding electromagnetic field. Specifically, the absorption rate of enantiomers under left- and right-circularly polarized light can be expressed as:

$$A^{\pm}=\frac{\omega}{2}\left(a_{\mathrm{ee}}^{''}|\boldsymbol{E}|^{2}+\mu_{0}^{2}a_{\mathrm{mm}}^{''}|\boldsymbol{H}|^{2}\right)\mp\frac{2}{\varepsilon_{0}}a_{\mathrm{em}}^{''}C, \tag{12}$$

where $a_{\mathrm{ee}}^{''}$, $a_{\mathrm{mm}}^{''}$, and $a_{\mathrm{em}}^{''}$ represent the imaginary parts of electric, magnetic, and magnetoelectric (chiral) polarizabilities of the chiral molecule, respectively. Since the CD arises from the differential absorption of left- and right-circularly polarized light, this yields a direct relationship between CD and optical chirality:

$$\mathrm{CD}=A^{+}-A^{-}=-\frac{4}{\varepsilon_{0}}a_{\mathrm{em}}^{''}C. \tag{13}$$

This finding highlights that CD is not an inherent molecular property alone but a coupled effect between molecular characteristics and the electromagnetic environment. By revealing this dependence, this work reshaped the theoretical framework of chiral detection enhancement and inspired extensive efforts aimed at engineering electromagnetic responses to generate optimal superchiral fields. Furthermore, their proposal of a standing-wave configuration offered an initial conceptual strategy for improving chiral detection sensitivity, which laid the foundation for subsequent experimental validations of superchiral light and related chiral detection enhancement schemes.

The chiral sensing using superchiral light was proposed in the same year (2010) using the metasurface[48], which will be introduced in detail in the metasurface part. Later in 2011, Tang et al. introduced fundamental research on the superchiral light, achieving an 11-fold enhancement in chiral discrimination over conventional circularly polarized light[49], as shown in Fig. 11. By reflecting circularly polarized light off a partially reflective mirror, the team generated standing waves with localized regions of extreme optical chirality density, amplifying the dissymmetry factor $g$ for chiral molecule excitation. Experimental validation used a nanofabricated sandwich structure to position chiral biperylene derivatives with sub-ångström stability, confirming enhanced dissymmetry ($g \approx 0.015$ vs. CPL's 0.0014) that aligned with theoretical predictions within 15%. This tunable technique enables stronger chiral sensing without near-field optics, with significant applications in pharmaceuticals and asymmetric synthesis.

Successively, various mechanisms to enhance the superchiral light have been proposed. Notable examples include plasmonics, nanocavities, metasurfaces, etc. Conventional methods such as SERS[201,202], have also evolved recently for chiral biomolecule detection. Especially, recent years have seen the integration of artificial intelligence in chiral sensing. In the next section, we will discuss these issues separately.

**Plasmonic-based chiral detection.** Plasmonics, the science of light manipulation at the nanoscale using metallic nanostructures, enables the generation of superchiral electromagnetic fields. These fields dramatically amplify chiral light matter interactions beyond conventional circularly polarized light, achieving significantly higher sensitivity for biomolecular detection. Plasmonics leverages metallic nanostructures (gold/silver nanoparticles, nanorods, dimers) as optical antennas to concentrate incident light into nanoscale hotspots, generating intense localized electromagnetic fields. Through deliberate geometric engineering, such as asymmetric gaps in nanoparticle dimers or chiral configurations, these structures manipulate the spatial relationship and relative phase between enhanced electric and magnetic field components. This precise phase control enables constructive interference that maximizes the vector product $\boldsymbol{E}\cdot\boldsymbol{H}$, directly amplifying optical chirality density ($C=-\omega\mathrm{Im}(\boldsymbol{E}^{*}\cdot\boldsymbol{H})/2c^{2}$) beyond conventional circularly polarized light. Unlike plane waves with fixed $\boldsymbol{E}$-$\boldsymbol{H}$ relationships, plasmonic hotspots create spatially varying superchiral fields where the localized optical chirality can exceed reference values for circularly polarized light in free space, $C_{0}=\pm\omega\varepsilon_{0}\boldsymbol{E}_{0}^{2}/2c^{2}$, by several orders of magnitude, fundamentally enabling nanoscale chirality manipulation unattainable with traditional sources.

Plasmon-enhanced chiral sensing offers transformative capabilities: massive signal amplification (enabling single-molecule detection and trace analysis of biomolecules), ultra-local probing below the diffraction limit (permitting spatial mapping of chirality in cellular microdomains or surface-confined systems), and versatile spectral tuning via nanostructure design. Critically, these plasmonic substrates integrate seamlessly with spectroscopic techniques such as SERS-enhanced circular dichroism and microfluidic lab-on-a-chip platforms, facilitating applications in pharmaceutical screening, amyloid disease diagnostics. This synergy of sensitivity, resolution, and compatibility establishes plasmonic superchiral light as a paradigm-shifting tool for advanced chiral biosensing.

Funck et al. engineered a DNA origami-based nanosensor functionalized with chiral gold nanorods to selectively bind and detect target RNA molecules via plasmonic CD

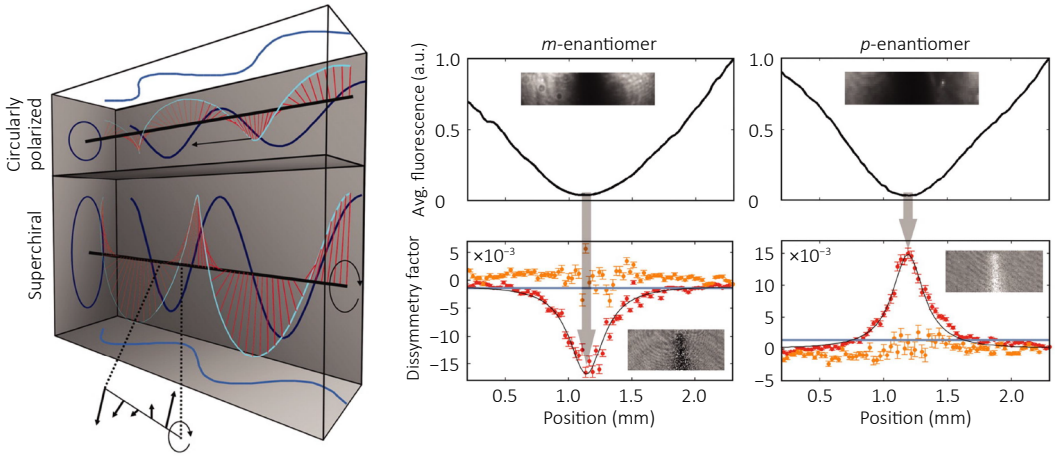



Fig. 11 | Early demonstration of superchiral light for enhanced chiral molecular detection. A standing-wave configuration formed by reflecting circularly polarized light from a mirror generates localized high-chirality hotspots, achieving an 11-fold sensitivity enhancement in chiral discrimination. Figure reproduced with permission from: ref.[49], AAAS.

modulation[203], as shown in Fig. 12(a). Enhanced chiral optical activity was observed when the sensor interacted with complementary RNA sequences, with a detection limit of 100 pM achieved under physiological conditions. This passive, amplification-free method[204–207] holds transformative potential for point-of-care diagnostics, enabling rapid, label-free detection of low-abundance viral RNAs (e.g., hepatitis C virus) in clinical samples with minimal sample preprocessing.

Rodier et al. demonstrated a novel method using chiral plasmonic nanostructures to detect the previously "invisible" chiral surface charge distributions of biomacromolecules like proteins[208], as shown in Fig. 12(b). This method successfully discriminates between structurally homologous proteins (type II dehydroquinase from different organisms), which are indistinguishable by conventional circular dichroism spectroscopy, by sensing differences in their chiral surface charge signatures manipulated via pH. It is a powerful tool for distinguishing between structurally homologous biomaterials and provides insights into macromolecular interactions.

Conventional plasmonic sensing faces challenges in achieving single-molecule chiral detection due to difficulties in gap size control, molecular orientation constraints, and the detrimental impact of quantum tunnelling on local field enhancement. To overcome these limitations, Zhang et al. designed a tunable chiral supramolecular plasmonic system combining helical oligoamide sequences and a nanoparticle-on-mirror resonator[209], as shown in Fig. 12(c). This system operates across classical and quantum regimes and significantly enhances chiral sensitivity in the quantum tunnelling regime, despite reduced local *E*-fields, due to strong Coulomb interactions between the chiral and light in the resonator and additional enhancement from tunnelling electrons. Consequently, the detection of a minimum of four molecules per single Au particle and the resolution of local enantiomeric excess within monolayers are demonstrated, pushing chiral sensing towards the ultimate single-molecule limit.

Plasmonics offers revolutionary advantages for chiral sensing, primarily through massive local field enhancement generated by nanostructures like nanoparticles, dimers, chiral structures, core-shells, or cavities[51,210–220]. This enables detection of ultra-low analyte concentrations (down to attomolar levels) and significantly amplifies weak intrinsic chiroptical signals (e.g., CD, ORD) via plasmon-coupled chirality. Plasmonic platforms also provide label-free, real-time detection and can discriminate structurally homologous biomolecules, which are inaccessible to conventional spectroscopy. Despite its high sensitivity, plasmonic chiral sensing faces critical challenges: quantum tunnelling effects in sub-nm gaps reduce local electric fields, diminishing signal enhancement; the nanostructures are difficult to fabricate and reproduce; background interference from non-specific binding disturbs measurement; a significant heating effect may do huge harm to biosamples and hinders practical biomedical applications. In contrast, a dielectric metasurface serves as a promising candidate for bio-friendly chiral sensing. In the following section, we will elaborate on this issue in detail.

**Nanophotonic and metasurface-based chiral detection.** A metasurface exploits subwavelength nanostructured arrays to precisely tailor light-matter interactions through local phase modulation and polarization control. These metasurface-based platforms offer transformative capabilities for electromagnetic field manpulation[221–233]. For instance, ultrabroad wavelength engineering, covering UV to THz regimes; deep subwavelength hotspot control, with size down to 10 nm; minimalized sensing devices with large-scale fabrication possibilities; biocompatible labelling, facili-

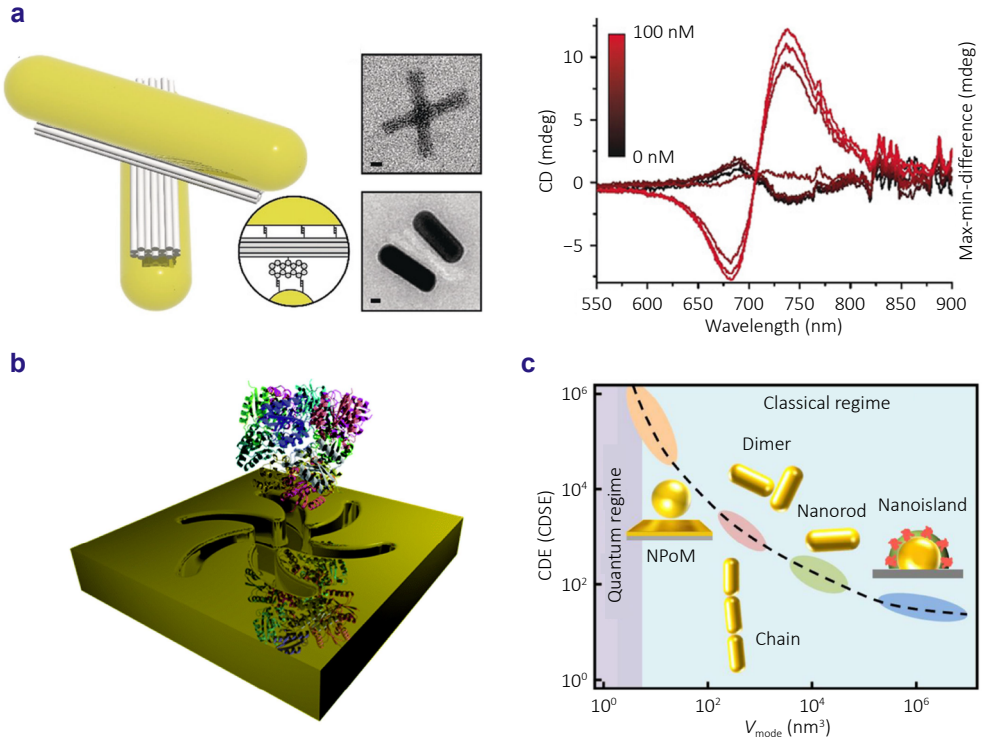



Fig. 12 | Plasmonic approaches for chiral detection. (a) DNA origami sensors functionalized with gold nanorods enabling RNA detection through plasmonic CD modulation. (b) Chiral plasmonic nanostructures probing subtle chiral surface charge distributions of proteins, which is invisible to conventional CD. (c) Supramolecular plasmonic resonators bridging quantum and classic regimes to achieve single-molecule chiral sensitivity[209]. Figure reproduced with permission from: (a) ref.[203], Wiley-VCH GmbH; (b) ref.[208], under a Creative Commons Attribution-Non Commercial 3.0 Unported Licence; (c) ref.[209], under the terms the Creative Commons CC BY license.

tating specific differentiation; integrable with quantum techniques, enabling entanglement-enhanced chiral sensing with huge signal-to-noise ratios.

Metasurface chiral sensing started with the first employment of the concept of "superchiral" light in 2010. Hendry pioneered ultrasensitive detection and structural characterization of chiral biomolecules using superchiral electromagnetic fields generated by plasmonic planar chiral metamaterials[48], as shown in Fig. 13(a). This novel principle leverages the dramatically enhanced chiral asymmetry within the near-fields of metamaterial, achieving differences in the effective refractive indices of chiral samples exposed to left- and right-handed superchiral fields that are up to $10^6$ times greater than those observed in conventional optical polarimetry measurements. As the first demonstration of superchiral fields for chiral sensing, this work established a ground-breaking biospectroscopy approach. It revealed unique sensitivity to specific biomolecular structures, such as $\beta$-sheets, opening a new paradigm for ultrasensitive bioanalysis. This has profound implications for detecting amyloid diseases and viruses, while fundamentally advancing nanophotonic chiral sensing by demonstrating tailored electromagnetic field chirality far exceeding the incident illumination.

Successively, Zhao et al. developed a novel approach using twisted plasmonic metamaterials with stacked achiral nanorod layers under relative rotation to amplify chiral interactions[234], as shown in Fig. 13(b). The major significance of this design is its ability to isolate and directly obtain the sign of molecular chirality using enantiomeric pairs of metamaterials (positive and negative 60-degree twist). After appropriate post-processing, this method enables unambiguous handedness detection while suppressing the large background CD signal inherent to shift-based methods. Furthermore, it achieves unprecedented sensitivity down to zeptomole levels ($10^{-21}$ mole), several orders of magnitude smaller than prior works. This work introduces an ultrathin, planarized nanophotonic interface designed to detect chiral molecules exhibiting inherently weak circular dichroism in the visible and near infrared spectral range.

These works with plasmonic structures achieve high sensitivity in chiral sensing[56,220,235–237], while having some limitations as discussed in the section plasmonic chiral sensing. An alternative solution is to design all-dielectric metasurfaces to avoid the potential heating effect. Solomon et al. pioneered one of the first dielectric metasurfaces (silicon nanodisk arrays) for chiral sensing and enantioselective separation, overcoming the limitation in plasmonic

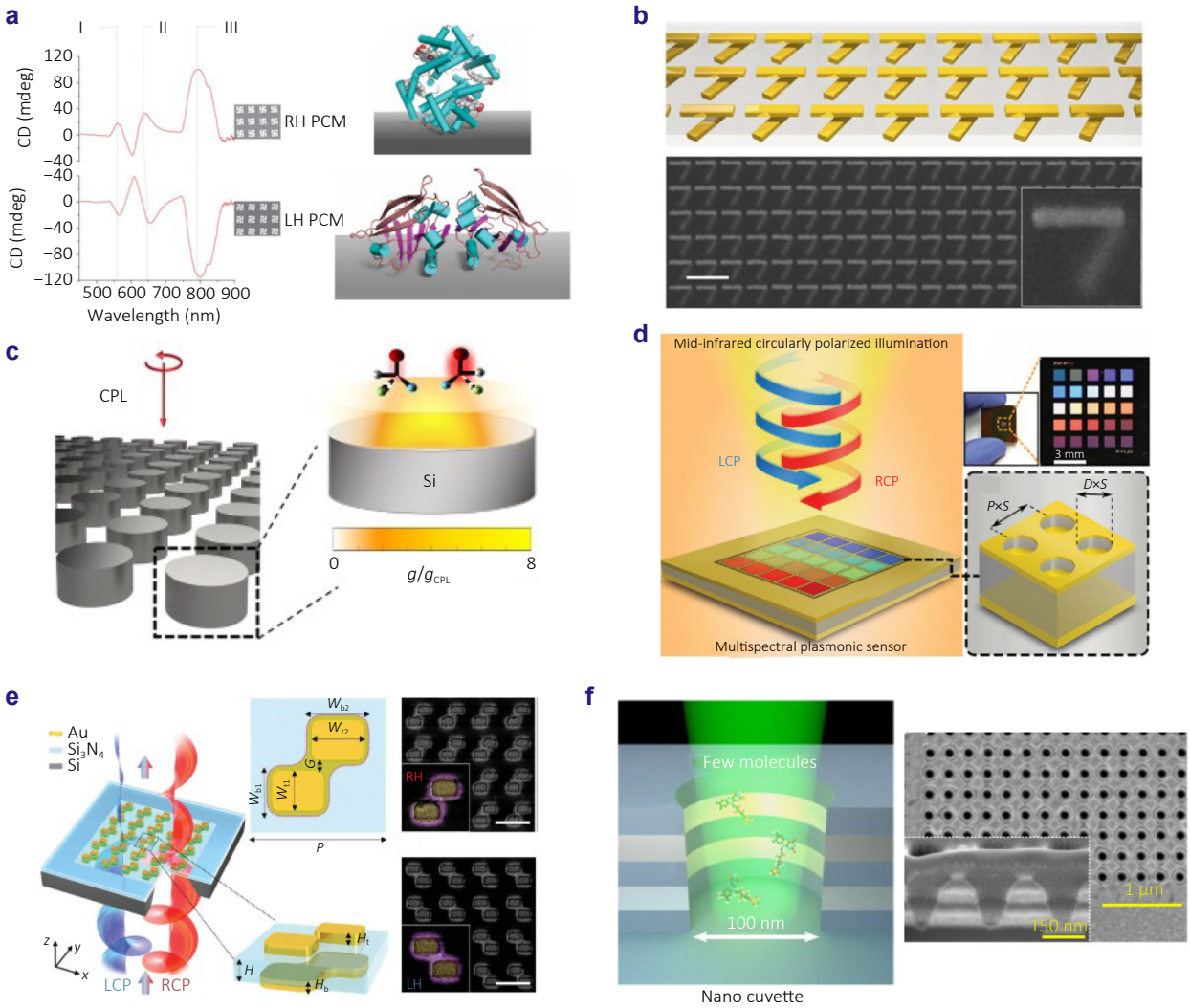



Fig. 13 | Metasurface-enhanced chiral sensing strategies. (a) Planar chiral metamaterials generating superchiral near fields for ultrasensitive biomolecular detection. (b) Twisted plasmonic metamaterials allowing zeptomole detection. (c) Dielectric metasurfaces leveraging Mie resonances for large-volume, low-loss chiral sensing. (d) Pixelated IR metasurfaces enabling vibrational chiral barcoding of molecular mixtures. (e–f) Suspended metasurfaces[253] and negative-index nanocavities achieving ultrathin and highly sensitive enantiodiscrimination. Figure reproduced with permission from: (a) ref.[48], Springer Nature; (b) ref.[234], under a Creative Commons CC BY license; (c) ref.[53], American Chemical Society; (d) ref.[239], Wiley-VCH GmbH; (e) ref.[253], Wiley-VCH GmbH; (f) ref.[240], American Chemical Society.

systems[53], as shown in Fig. 13(c). By leveraging Mie resonances and Kerker conditions to spectrally overlap electric and magnetic modes, the uniform sign and large volume enhancements in optical chirality density and Kuhn's dissymmetry factor can be achieved. This enables enantiopure interactions across the entire metasurface, facilitating practical chiral separation. The platform has an increase in yield by a factor of >2000 for visible wavelength photoionization reactions while maintaining field intensities, offering a scalable, low-loss solution for efficient all-optical resolution of racemic mixtures.

Building upon this foundation, subsequent studies have advanced the concept from detecting single-species enantiomers to identifying complex mixtures, and from UV-Vis based measurements to VCD detection. More recently, Biswas et al. demonstrated surface-enhanced infrared absorption-induced VCD detection of thalidomide at ultralow concentration down to 50 μM using an achiral plasmonic system[238]. The experiments revealed a remarkable 13 orders of magnitude enhancement in sensitivity compared to conventional far-field VCD techniques. Successfully, this approach was further generalized by arraying the nanostructures into pixelated patterns across a broad infrared range, thereby enabling the simultaneous interrogation of multiple chiral species[239], as shown in Fig. 13(d). By exploiting the distinct vibrational absorption "fingerprints" of different molecules, this strategy realizes a unique chiral "barcoding" scheme capable of reliably identifying and distinguishing

enantiomers and biomolecules. Collectively, these advances highlight the potential for achieving high-sensitivity chiral detection in realistic molecular mixtures, making a significant step toward real-world applications.

In the past few years, more and more elegant and intriguing metasurface architectures have been proposed to expand the capabilities and increase the sensitivities in chiral sensing. For instance, nanocavities[56,240–244], special particles[217,245–250] (e.g., core-shell, upconvention, etc), layered structures[45,251–261], achiral designs[20,53,244,262–266], and so forth[267–269].

Unlike Zhao's design with aligned plasmonic structures[234], Cen et al. developed ultrathin self-aligned suspended chiral metasurfaces using single-step electron beam lithography to achieve globally enhanced optical chirality[253], as shown in Fig. 13(e). Label-free enantio-discrimination at the zeptomole level was experimentally demonstrated, enabled by bidirectional molecular exposure and near-field plasmonic coupling. Leveraging giant chiroptical response, this metadevice enables ultrathin circular polarizers, chiral molecular sensing, and chiral information processing. Recently, Indukuri et al. engineered achiral negative-index metamaterial nanocavities to generate globally enhanced, enantiopure superchiral fields for fluorescence-detected circular dichroism sensing[240], as shown in Fig. 13(f). CD measurements can be significantly enhanced through background-free detection of flavin mononucleotide chiral molecules, validated by 8-fold enhanced fluorescence decay rates and spatial uniformity in dissymmetry factors (~0.1). This breakthrough enables single-molecule chiral sensing by overcoming intrinsic background limitations of chiral plasmonic structures, with transformative implications for pharmaceutical screening and point-of-care diagnostics.

More recently, qBIC have attracted increasing attention in chiral detection[56,270–273]. Compared with ideal BICs, qBIC modes introduce controlled radiation leakage, resulting in ultrahigh but finite quality factors that are more accessible in practical implementations. The strong field confinement and enhanced optical chirality associated with qBIC modes enable substantial amplification of chiroptical signals, offering promising opportunities for ultrasensitive chiral sensing. Nevertheless, the performance of qBIC-based platforms remains sensitive to fabrication imperfections and environmental perturbations, which poses challenges for scalable and robust applications. More recently, qBIC have attracted increasing attention in chiral detection[56,270–273]. Compared with ideal BICs, qBIC modes introduce controlled radiation leakage, resulting in ultrahigh yet finite quality factors that are more accessible in practical implementations. The strong field confinement and enhanced optical chirality associated with qBIC modes enable substantial amplification of chiroptical signals, offering promising opportunities for ultrasensitive chiral sensing. For example, Chen et al. have demonstrated a BIC metasurface capable of integrated acquisition of CD spectrum and molar concentration over a single metasurface[56] with high sensitivities, as shown in Fig. 14(a). Li et al. proposed a new paradigm for ultrasensitive chiral detection by creating accessible chiral hotspots using a toroidal dipole Fabry-Perot bound state in the continuum (TD FP-BIC) metasurface[270], achieving ultrahigh optical chirality enhancements of up to $10^4$-fold (Fig. 14(b)). The emergence of TD FP-BIC originates from destructive interference between TD resonance and the multilayer reflector-induced perfect mirror image. More intriguingly, the complex-valued Pasteur parameter, has been recently proved to induce strong coupling between two BICs in a metasurface (Fig. 14(c)), mediated by both the real[271] and imaginary[273] components of the Pasteur parameter. Nevertheless, the performance of qBIC-based platforms remains sensitive to fabrication imperfections and environmental perturbations, which poses challenges for practically and robust applications.

For special particles, Huang et al. proposed passivated aluminum chiral shells via colloidal self-assembly to create ultraviolet plasmonic biosensors with uniform superchiral fields and surface lattice resonance modes[274], as shown in Fig. 15(a). Record-breaking chiral sensor performance was demonstrated with the chiral sensor parameter reaching 10.9095 for the null point and 0.1739 for peaks of *g*-factor spectra, enabled by narrowed resonance linewidths. This platform also achieves zeptomole-level enantiomer discrimination, advancing label-free chiral sensing for biomedical diagnostics and pharmaceutical quality control. Manoccio et al. developed a core-shell 3D chiral metamaterial biosensor by combining platinum nanohelices with a conformal polymer coating, creating polarization-dependent optical responses that minimize background interference in complex biological environments[246]. Femtomolar sensitivity (10 fM) was demonstrated through redshifted CD spectra, achieving a 27 nm/pM sensitivity slope for TDP-43 biomarker detection in neurodegenerative diseases. This platform enables label-free, chip-based detection in human serum with unprecedented specificity, advancing point-of-care diagnostics. Upconversion nanoparticles can endow intriguing nonlinear effects. Lee et al. developed an upconverting chiral metamaterial platform that leverages nonlinear optical processes to amplify enantiomer discrimination signals[245], as shown in Fig. 15(b). Small CD differences in near-infrared were converted into amplified visible photoluminescence contrasts via embedded core-shell upconversion nanoparticles, enabling detection of D-/L-glucose enantiomers at 0.05-M concentration. This nonlinear transduction strategy overcomes intrinsic sensitivity limitations of chiral sensing by exploiting power-dependent upconversion to resolve previously undetectable chirality signatures, advancing label-free molecular diagnostics for pharmaceuticals and biochemistry[247,275].

**SERS-based chiral sensing.** SERS leverages enhanced electromagnetic fields near plasmonic nanostructures to achieve extraordinary signal amplification ($10^6$ to $10^{14}$ fold) and single-molecule sensitivity. This technique captures

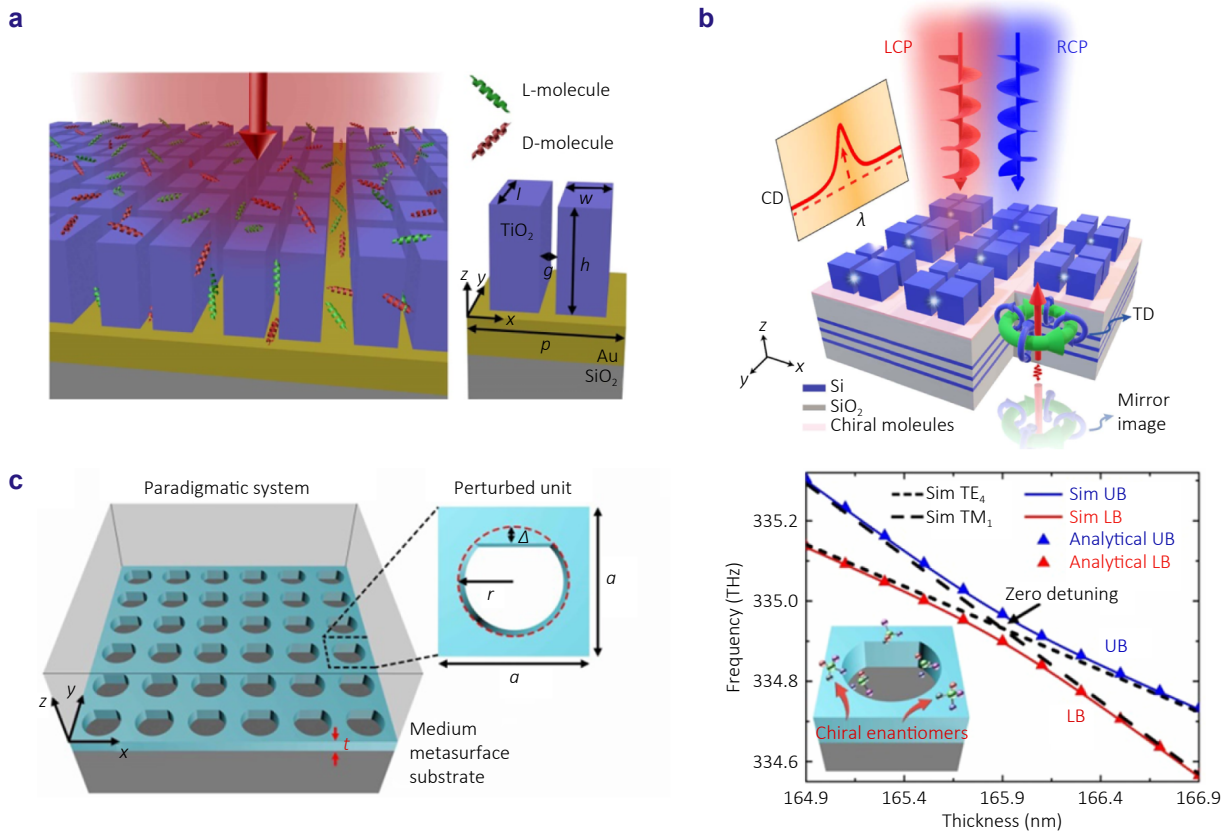



Fig. 14 | qBIC metasurface-based chiral sensing strategies. (a) Hybrid metasurface enabling the integrated detection of CD spectrum and molar concentration. (b) TD FP-BIC metasurface consisting of a dielectric metasurface and a multilayer reflector separated by a dielectric spacer. (c) High-Q coupling metasurface assisted by externally introduced enantiomers of weak chirality. Figure reproduced with permission from: (a) ref.[56], American Chemical Society; (b) ref.[270], Optica Publishing Group; (c) ref.[273], American Physical Society.

molecular fingerprints via Raman peaks, making it ideal for chiral sensing applications that demand precise discrimination of enantiomers. In the past few years, SERS have been widely utilized for chiral sensing, achieving unprecedented performance. The first demonstration to use SERS for chiral sensing was proposed by Zhang et al., who utilized the self-assembled core-satellite gold nanoparticle network. Based on the changes in the tunnelling current, this approach was able to identify the chirality of carnitine molecule with nanomolar concentration[52]. Wang et al. developed a chiral-label-free SERS strategy using vertically aligned Au nanorod arrays to synchronously discriminate and identify small aromatic enantiomers without chiral auxiliaries or circularly polarized light[276], as shown in Fig. 16(a). This approach enables ultrasensitive chiral sensing with molecular specificity, successfully identifying >10 chiral compounds (e.g., amino acids, alcohols) and offering transformative potential for real-time analysis in pharmaceutical synthesis and asymmetric catalysis.

Fundamentally, an ideal chiral discrimination strategy is difficult to achieve due to the inevitable nonspecific binding of wrong enantiomers and the insufficient intrinsic optical activity of chiral molecules. To address this issue, Arabi et al. engineered an "Inspector Recognition Mechanism" for absolute chiral discrimination using SERS with chiral-imprinted polydopamine substrates[277], as shown in Fig. 16(b). Specific enantiomer binding is verified by linear aminothiol inspectors, which degrade SERS tags only when imprinted cavities are vacant or non-specifically occupied, while fully occupied cavities block inspector permeation. This strategy achieves ultrahigh sensitivity (limit of detection: $10^{-5}$–$10^{-4}$ μg·L$^{-1}$) along with broad enantioselectivity across diverse chiral analytes, enabling direct analysis in complex biological/environmental matrices. Leong et al. developed a generic method for chiral distinguishment using SERS[278], as shown in Fig. 16(c). This method utilizes a label-free chiral SERS sensing strategy by synergizing nanoporous gold bowls with electrochemical modulation to generate enantiospecific molecular fingerprints. Intrinsic surface defects on gold bowls act as asymmetric recognition sites, enabling stereospecific enantiomer adsorption without chiral probes. Consequently, the direct enantiomeric differentiation is achieved, validated by unique spectral signatures and chemometrics.

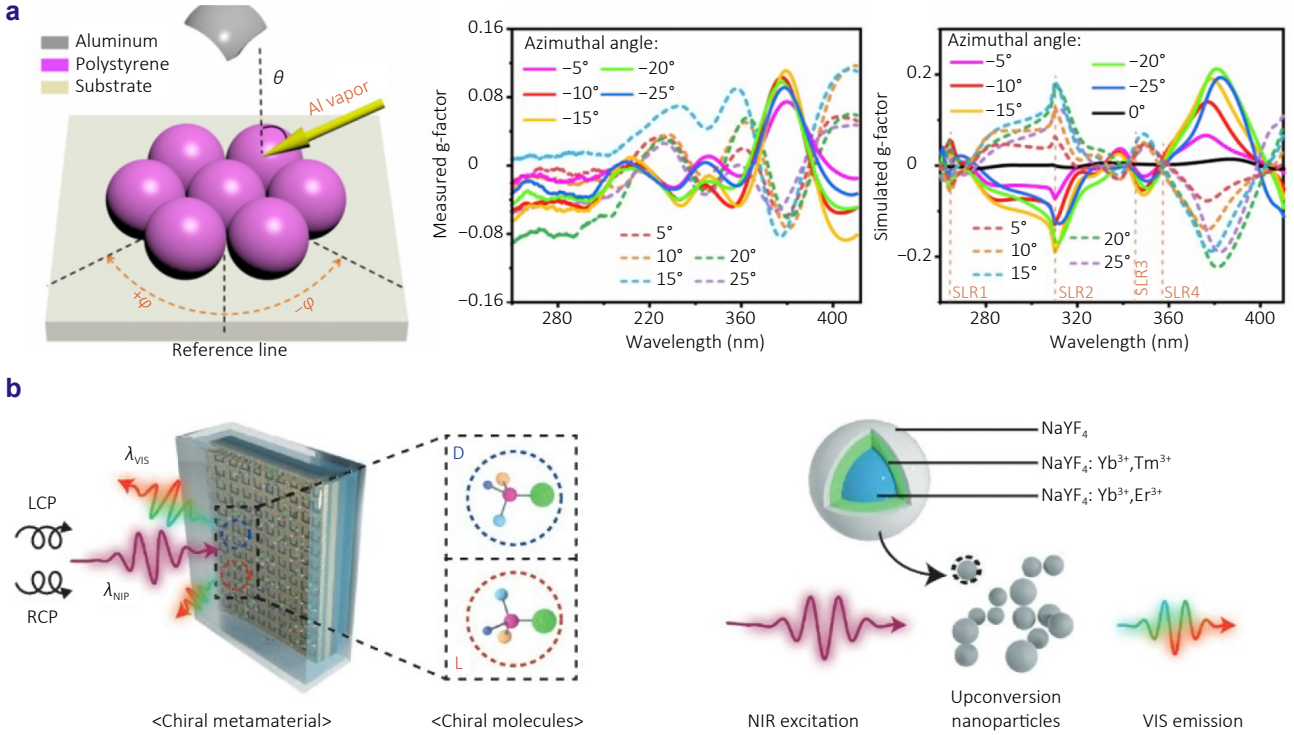



Fig. 15 | Nanoparticle-enhanced chiral sensing strategies. (a) Core-shell metamaterials based ultrasensitive ultraviolet chiral plasmonic biosensor. (b) Upconversion nanoparticles extending sensitivity from femtomolar to nonlinear detection regimes. Figure reproduced with permission from: (a) ref.[274], American Chemical Society; (b) ref.[245], Wiley-VCH GmbH.

SERS chiral sensing uses molecule-specific vibrational fingerprints for label-free enantiomer differentiation[279–285], offering versatile chiral sensing for pharmaceuticals and biomedicine[57,286–289]. It achieves ultrahigh sensitivity through plasmonic enhancement and avoids extrinsic chiral selectors by employing engineered, intrinsically chiral nanostructures. These nanostructures create localized asymmetric environments that drive stereospecific adsorption. However, the field may intrinsically face some limitations: susceptibility to matrix interference in biological samples, challenges in scalable nanofabrication of reproducible chiral substrates, and restricted analytical throughput for multiplexed detection due to spectral complexity. Future efforts could likely be devoted to, for instance, machine learning-enabled spectral deconvolution for real-time enantiomer identification in complex matrices; miniaturized lab-on-chip systems enabling point-of-care deployment for clinical diagnostics. These efforts aim to bridge fundamental nanomaterial innovations with practical applications requiring precise chiral discrimination.

**AI-assisted chiral detection.** When analyzing complex multicomponent samples, subtle enantiomeric differences in optical spectra (e.g., peak shifts, intensity ratios) are often obscured by noise or matrix interference. ML provides a powerful means to extract these latent patterns, which are undetectable by conventional analysis, and has already been widely employed across various scientific disciplines[148,290–305]. Owing to its strong target-recognition capabilities, ML can analyze spectrum signals of specific chiral molecule and even directly identify the geometric handedness of chiral particles.

Traditional approaches typically rely on imaging or spectral data of chiral molecules[306–310], employing methods such as support vector machines, fully-connected neural networks, or random forests for classification and identification. However, these methods often struggle with the high dimensionality and information-rich nature of raw data, leading to poor recognition performance when the data is insufficient. Dimensionality reduction techniques, such as principal component analysis, are commonly applied to address this issue[311], yet they still require manual feature extraction and careful selection of principal components.

In contrast, deep learning leverages deep neural networks to automatically perform feature extraction[312]. Convolutional neural networks[313,314] (CNNs), as a core deep learning architecture, can process both one-dimensional spectral and two-dimensional imaging data. By applying convolutional kernels to extract image features, CNNs effectively reduce data dimensionality and are typically connected to fully-connected neural networks to perform classification. Variants such as VGG and ResNet exhibit powerful image recognition capabilities and are readily adaptable for chiral molecule recognition. For data affected by significant background noise, specialized architectures like YOLO or U-Net

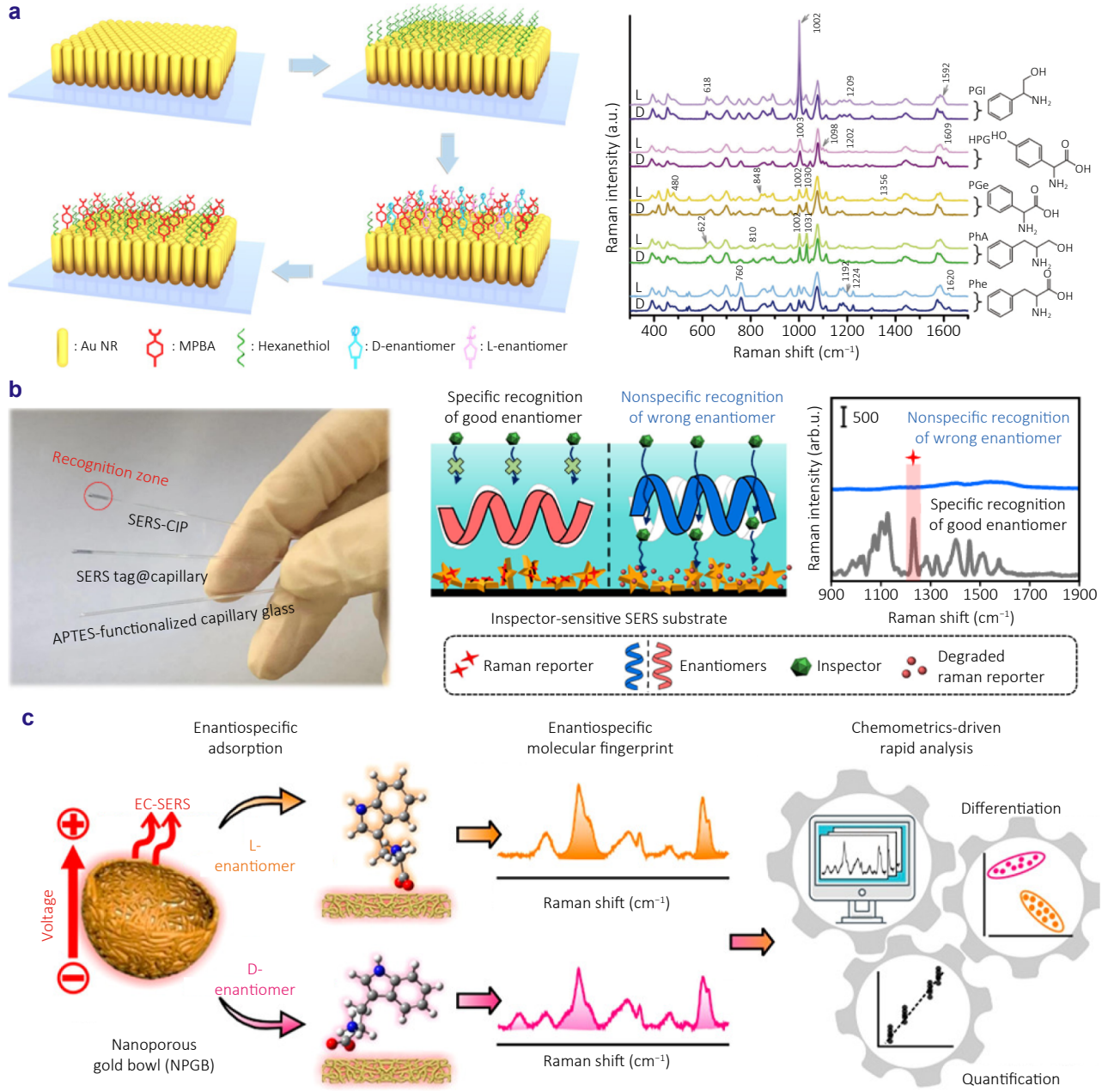



Fig. 16 | SERS-enabled chiral sensing strategies. (a) Label-free SERS using vertically aligned Au nanorod arrays for molecular enantiomer discrimination. (b) Chiral-imprinted polydopamine substrates combined with inspector molecules enabling absolute chiral discrimination with ultrahigh sensitivity. (c) Nanoporous gold bowls coupled with electrochemical modulation to realize stereospecific enantiomer absorption and molecular fingerprinting. Figure reproduced with permission from: (a) ref.[276], Wiley-VCH GmbH; (b) ref.[277], under a Creative Commons CC BY license; (c) ref.[278], American Chemical Society.

can be applied for object localization and image segmentation, extracting small regions containing only the target, which are then fed into classification networks for chiral molecule identification.

The use of *R*-CNN for chiral particle recognition represents an important milestone in automated molecular analysis. *R*-CNN identifies and classifies chiral structures from scanning tunnelling microscope (STM) images, however, their multi-stage pipeline limits efficiency. Faster *R*-CNN[315] improve upon this by unifying region proposal, feature extraction, and classification into a single network. This evolution significantly improves both inference speed and training efficiency while maintaining high recognition accuracy.

The approach used in the ref.[315] consists of the following four components: data selection, data augmentation, model training, and domain-specific expertise. The data selection module employs *t*-SNE to evaluate data quality and visual-

ize molecular image distributions, facilitating the curation of high-quality training samples. The data augmentation module expands the dataset using synthetic variations of raw STM images. The model training module adopts Faster *R*-CNN, which performs feature extraction, molecule detection, and chiral classification in an end-to-end manner. The fourth module incorporates domain knowledge through conditional random fields to refine predictions on low-quality STM images, reducing false positives and improving overall recognition performance. Once fully trained, the pipeline automatically processes hundreds of STM images across varying resolutions, with each chiral molecule annotated by a bounding box and its corresponding chiral class.

Recently, Han et al. developed a deep-learning-enabled methodology combining neural networks with genetic algorithms to predict and inversely design the chiroptical properties of plasmonic Born-Kuhn nanodimers for target-specific chiral sensing[316], as shown in Fig. 17(a). The optimal sensor structure was algorithmically optimized by the genetic algorithm based on neural-network-predicted circular dichroism spectra, enabling ultrasensitive enantiomer discrimination without chiral probes. This approach establishes a versatile platform for designing chiral plasmonic sensors tailored to specific analytes, advancing precision in pharmaceutical and biomedical diagnostics. Using linear programming and a parameter sweep algorithm[55], Santos et al. quantified the concentration and relative proportions of all four stereoisomers in 20 samples with diverse isomeric distributions, achieving an average absolute percent error of 1.7%.

Reinforcement learning enables resource-efficient optimization by autonomously exploring parameter spaces through trial-and-error interactions with an environment, strategically prioritizing high-potential nanostructures over exhaustive simulation. Chen et al. developed a reinforcement-learning-driven workflow integrating neural networks and Bayesian optimization to inversely design chiral plasmonic metasurfaces with sharp CD peaks[304]. With this approach, fabricated microfluidic chips are capable of differentiating glucose enantiomers via 7-nm resonance shifts, as validated by cathodoluminescence spectroscopy. This method establishes a demonstrably effective framework for algorithmically evolving nanophotonic sensors, significantly advancing label-free chiral detection in biomedicine while minimizing computational costs. Notably, Zhang et al. developed a deep-learning framework with a cyclic data iteration strategy that significantly outperforms prior methods by expanding the chiral metasurface design space to 30×30-pixel freeform structures while achieving a 21-fold increase in high-CD-response (>0.6) yield[317]. The methodology's efficacy was experimentally validated through terahertz biosensing, where record-high simulated/experimental CD values (≈0.7/0.6) were attained, enabling label-free differentiation of D/L-glutamic acid enantiomers with 0.08 CD resolution. This approach establishes a universal pipeline for calibration-free chiral detection, overcoming computational bottlenecks in nanophotonic design and accelerating clinical translation for disease diagnostics and drug development.

Chiral particles exhibit geometric handedness almost indistinguishable to the human eye. Machine learning can analyze microscopy images to classify this handedness. Visheratina et al. developed a deep learning framework combining Siamese learning and synthetic data generation to identify chirality in scanning electron microscope (SEM) images with minimal training data[318], as shown in Fig. 17(b). Using only 30 original images, it achieved near-perfect (99%) accuracy for detecting chiral bowtie particles and distinguishing their handedness. The model generalized effectively, reaching 93% accuracy on unseen chiral geometries without retraining. This approach enables high-throughput, automated chirality analysis of nanostructured materials, overcoming traditional EM limitations and accelerating discovery for photonic and biomedical applications. Later, Huang et al. developed an automated deep learning framework using Grounding DINO, Segment Anything, and ResNet to achieve 99% accuracy in chiral nanoparticle segmentation and handedness classification from SEM images, requiring zero manual annotations[319], as shown in Fig. 17(c). By leveraging Grounding DINO and Segment Anything for automated detection and segmentation, this approach eliminated manual annotation entirely and reduced data requirements by 33% compared to prior methods, achieving high accuracy with only 20 raw SEM images versus over 30 labelled images. Crucially, synthetic data augmentation enabled robust handling of overlapping particles, resolving a key limitation in earlier segmentation models while maintaining greater than 95% accuracy across resolutions for high-throughput screening.

Overall, optical chiral detection has evolved from conventional far-field spectroscopic techniques toward nanophotonic-enhanced and data-driven sensing paradigms. Traditional chiroptical methods provide a solid physical foundation for enantiomer identification, while nanophotonic platforms, such as plasmonic structures, dielectric metasurfaces, and BIC resonators, enable strong field confinement and enhanced optical chirality, significantly amplifying weak chiroptical signals. These advances have greatly improved detection sensitivity, yet they also introduce new challenges, including fabrication sensitivity, environmental perturbations, stringent experimental conditions, and the increasing complexity and dimensionality of experimental data.

In this context, deep-learning-based approaches have begun to play a substantive role in chiral molecule detection by enabling the identification of weak and complex chiroptical signatures that are difficult to resolve using conventional analytical models. In particular, neural networks have shown promise in enhancing detection sensitivity, improving classification robustness, and accelerating the interpretation of high-dimensional spectral data in chiral sensing platforms.

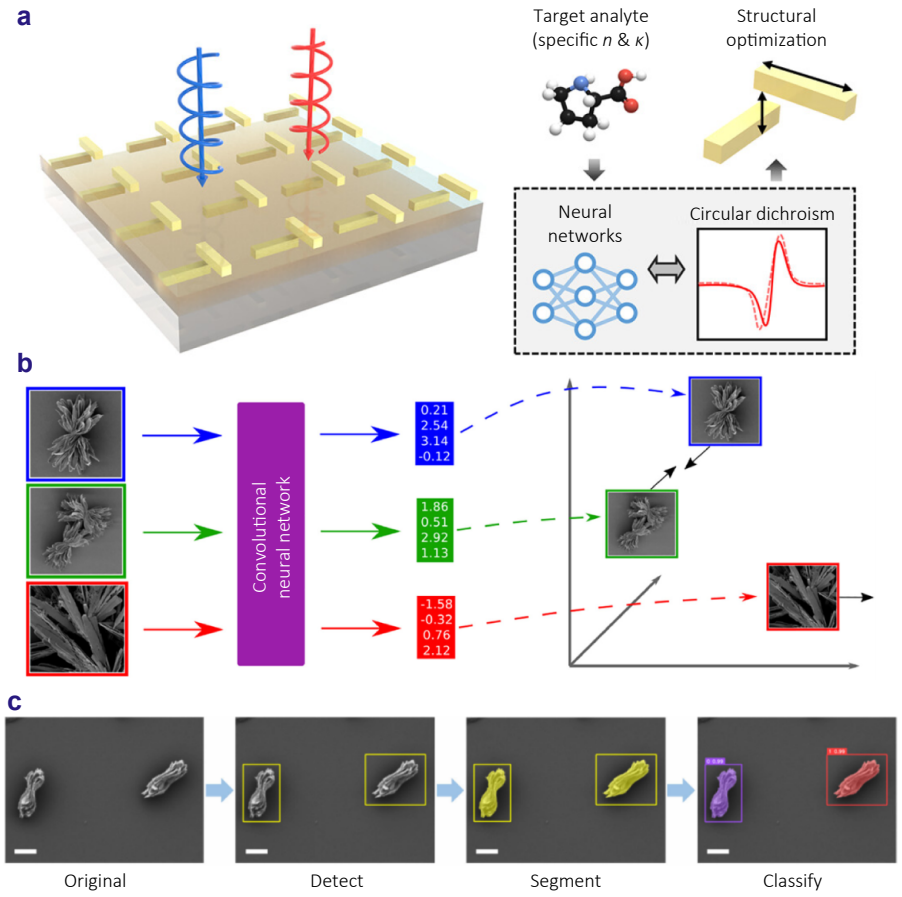



Fig. 17 | Artificial intelligence in chiral detection. (a) Neural network-guided genetic algorithms for optimizing plasmonic nanodimer sensors, enabling ultra-sensitive enantiomer discrimination. (b) Deep learning models employing Siamese architectures to identify nanoparticle handedness directly from SEM images. (c) Automated segmentation and classification pipelines integrating Grounding DINO, Segment Anything, and ResNet, achieving high-throughput and annotation-free analysis of chiral nanoparticles. Figure reproduced with permission from: (a) ref.[316], American Chemical Society; (b) ref.[318], American Chemical Society; (c) ref.[319], American Chemical Society.

However, the application of deep learning in chiral molecule detection faces several major challenges, with the most significant being the scarcity of high-quality and accurately labelled datasets. Chiral identification requires expert annotation and experimental validation, which are both time-consuming and costly. As a result, available datasets are often limited in size. When trained on such small-scale data, deep neural networks are prone to overfitting, leading to strong performance on training data but poor generalization to new samples. Additionally, structural variability and noise in real-world data further complicate model training and reliability.

Future developments in AI-assisted chiral detection will likely focus on four key directions. (1) Generative models, including generative adversarial networks and diffusion models, offer a promising route to augment chiral spectral and light-matter interaction datasets, thereby alleviating data scarcity and improving model robustness in low-sample regimes. (2) Self-supervised, semi-supervised, and few-shot learning strategies are particularly well suited for chiral detection tasks, where labelled enantiomeric data are scarce and costly to obtain. (3) The incorporation of domain knowledge and physics-inspired constraints, such as symmetry considerations and chiroptical response models, into network architectures can improve training efficiency while enhancing physical interpretability and generalization across different chiral systems. (4) Multimodal learning frameworks that integrate spectral, structural, and chemical descriptors are expected to further improve the robustness and interpretability of chiral recognition systems, especially for complex or weakly chiral molecular targets.

## 4 Conclusions

Over the past decade, optical sorting and detection of chiral molecules have undergone rapid progress, driven by advances in structured light fields, nanophotonic devices, and integrated systems. Detailed comparisons of representative methods, including their key performance metrics and application scenarios, are summarized in Tables 1–3. Never-

theless, this field remains at a formative stage, with substantial room for improvement and several significant challenges to be addressed, as schematically illustrated in Fig. 18.

For optical sorting, research has evolved from early demonstrations based on ORP, OGF, OLF and OPF to more sophisticated platforms such as metasurfaces, waveguides, BICs and EPs. While these approaches are steadily advancing enantioselective manipulation toward higher precision, speed, versatility, and biocompatibility, practical deployment remains constrained by several fundamental and technical challenges, most notably low throughput and insufficient system stability. More specifically, low throughput in optical chiral sorting fundamentally arises from the intrinsic trade-off between optical force magnitude and interaction range. High-$Q$ near-field platforms, such as BICs and EPs based nanophotonic structures can generate strongly enhanced optical forces, but their effective working distance is typically confined to subwavelength scales. In contrast, far-field optical forces offer larger interaction ranges but are generally too weak for efficient enantioselective manipulation. Strategies that enhance near-field force efficiency while extending the effective interaction region seems feasible, but they require further development and deeper exploitation of resonant mechanisms such as BICs and EPs. In addition, optical force-based sorting places stringent demands on system stability. Optical heating, thermal diffusion, and background noise can readily degrading performance. Integrating optical manipulation with advanced microfluidic platforms[320–323] offers a promising route to improved stability and environmental control, although challenges related to flow regulation, interface engineering[324], co-design of microfluidic and nanophotonics, and long-term stability under realistic operating conditions remain to be addressed. From a commercialization perspective, additional constraints must be considered. At the microscale, optical sorting offers limited advantages compared with mature techniques such as flow cytometry and acoustic sorting. At the nanoscale, practical deployment is hindered by low sorting throughput, the high fabrication cost of large-area near-field structures, limited chip reusability, and insufficient long-term operational stability. Addressing these challenges will be essential for translating optical chiral sorting from proof-

Table 1 | Performance comparison of different chiral sorting methods.

| Technology | Particle types | Size ($d$) | Speed | Limitation | Experiment (E)/ Theory (T) | Ref. |
|---|---|---|---|---|---|---|
| Optical radiation pressure | Cholesteric droplet | 20–30 μm | 10–50 μm·s$^{-1}$ | Difficult for nanosized particles | E | ref.[110] |
| Optical gradient force | Polymer | 40–50 nm | Quasi-static | Limited size range | T | ref.[139] |
| Optical pulling force | Polymer | 0.2–1 μm | Quasi-static | Specific size | T | ref.[133] |
| Optical lateral force | Cholesteric droplet | 0.2–20 μm | Quasi-static | Multi-force control | E | ref.[129] |
| Vector beams | Polymer | 100–500 nm | Quasi-static | Limited size range | T | ref.[134] |
| Waveguide | Polymer with mild absorption | 4–40 nm | Quasi-static | Limited size range | T | ref.[43] |
| metasurface | Polystyrene | 20–200 nm | 800 μm·s$^{-1}$ | Require tunable lasers and elegant chip design | T | ref.[45] |
| Metasurface with BIC | Polystyrene | 20 nm | Quasi-static | Size-sensitive structure | T | ref.[175] |
| Metasurface with EP | Polymer | 8 nm | Quasi-static | Size-sensitive structure | T | ref.[179] |

Table 2 | Performance comparison of different chiral sensing methods.

| Technology | Configurations | Sample | Sensitivity | Time | Limitation | Ref. |
|---|---|---|---|---|---|---|
| Plasmonics | Single particles | RNA | 100 pM | 30 min | May be affected by the incubation | ref.[203] |
| | Nanostructures | Flavin mononucleotide | A few tens of molecules | Time-resolved | Complex structure | ref.[240] |
| | Quantum regime | Oligoamide sequences | Single molecules | > 12 h | Time consuming | ref.[209] |
| Metasurface | Single-layer metallic | Phenylalanine | 10 μM | Time-resolved | Complex structure | ref.[329] |
| | Dual-layer metallic | Aspartic acid | 0.1 mg/mL | Time-resolved | Complex structure | ref.[253] |
| | Dielectric | Phenylalanine | 5 μg/mL | Time-resolved | Limited enhancement | ref.[266] |
| | Core-shell | TAR DNA-binding protein 43 | 27 nm/pM or 10 fM | 5–6 h | Complex chemical treatment | ref.[246] |
| | Nonlinear | Glucose | 0.05 M | Time-resolved | High power requirement | ref.[245] |
| SERS | Particles | 42-residue-long amyloid-$\beta$ fibrils | $4 \times 10^{-15}$ M | Time-resolved | Costly | ref.[57] |
| | Structures | Glucose | $8 \times 10^{-10}$ M | Time-resolved | Costly | ref.[282] |
| Machine learning | Spectra | Glutamic acid | 0.1 mg/mL | Time-resolved | Complex structure | ref.[317] |
| | Shape | Complex microparticles | Single particles | Offline (image-dependent) | Size- and phase-limited | ref.[318] |

Table 3 | Performance comparison of optical chirality enhancements across representative nanophotonics platforms.

| Technology | Configurations | Wavelength(nm) | Optical chirality enhancement | Limitation | Ref. |
|---|---|---|---|---|---|
| Metasurface | Nanodisk | 1219 | 138 | Limited enhancement | ref.[53] |
| | Nanoresonator | 700 | 25 | Limited enhancement | ref.[330] |
| | Achiral dielectric metasurface | 550 | 30 | Limited enhancement | ref.[266] |
| | Anapole metasurface | 600 | 140 | Limited enhancement | ref.[244] |
| | QBIC $TiO_2$ dimer | 860 | 247 | Sensitive to fabrication | ref.[56] |
| | Coupling BIC metasurface | 900 | - | Sensitive to fabrication and environment | ref.[273] |
| | QBIC Si dimers | 1300 | 10000 | Sensitive to fabrication | ref.[175] |
| Plasmonics | Planer chiral metamaterials | 800 | 12 | Complex structure<br>Background CD | ref.[48] |
| | Racemic nano plasmonic arrays | 700 | 7 | Complex structure<br>Photothermal heating | ref.[268] |
| Nanocavity | Nanocuvettes | 460 | 10 | Limited enhancement | ref.[240] |
| | Optical cavities | 532 | 2200 | Complex structure | ref.[331] |
| Nanoparticle | Aluminum chiral shells | 375 | 12 | Limited enhancement<br>Complex structure | ref.[274] |

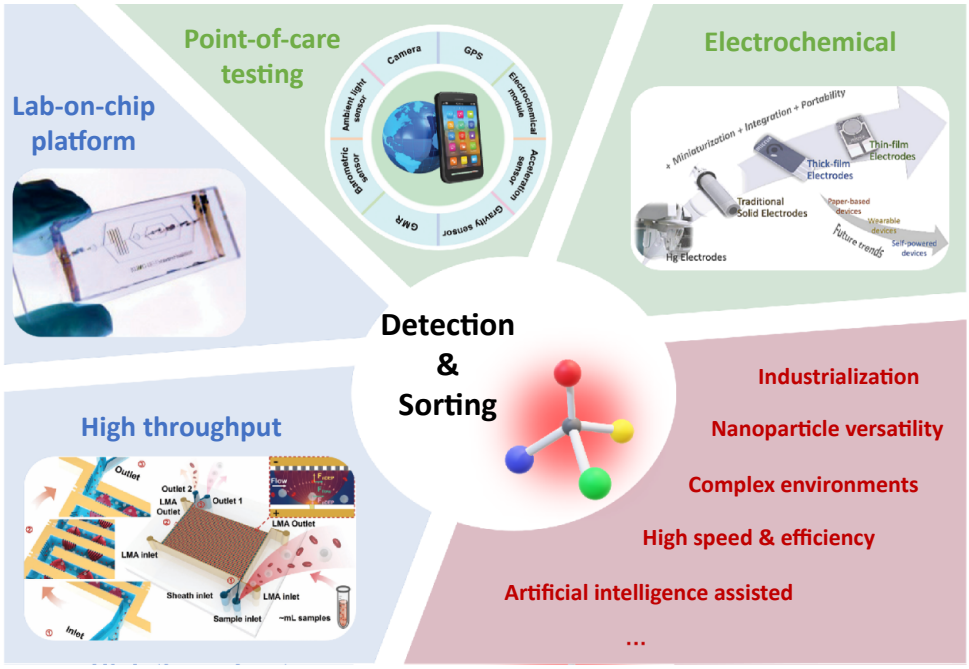



Fig. 18 | Schematic illustration of future prospects in chiral optical sorting and detection. For sorting, key directions include integration with microfluidic systems, development of lab-on-chip platforms[323], and achieving high-throughput[328] enantioselective separation. For detection, research is advancing toward point-of-care testing[325] and hybrid multimodal strategies[327] for more efficient measurements. In addition, large-scale industrialization, broad nanoparticles versatility across diverse physical properties, adaptation to complex real-world environments, high speed and efficiency, and AI-assisted data analysis and the pursuit of faster, more reliable operation represent common goals for both sorting and detection. Figure reproduced with permission from: ref.[323], Royal Society of Chemistry; ref.[325], Wiley-VCH GmbH; ref.[327], Elsevier B.V.; ref.[328], Wiley-VCH GmbH.

of-concept demonstrations toward practical applications.

For chiral detection, techniques including superchiral fields, plasmonic and dielectric metasurfaces, VCD, and SERS have substantially boosted sensitivity, in some cases enabling detection down to the single-molecule and zepto-mole levels. However, similar to optical sorting, these approaches are fundamentally constrained by intrinsic physical trade-offs between near-field enhancement, effective interaction range, and measurement robustness. While strong near-field confinement enables extreme sensitivity, it often comes at the cost of limited probing volume, stringent fabrication tolerances, and increased susceptibility to environmental perturbations. In addition, chiral optical detection generally lacks intrinsic molecular specificity, which

poses further challenges for identifying target chiral species in complex real-world environments, such as serum or urine, where multiple chiral and achiral components coexist. Addressing this issue typically requires complementary strategies, including surface functionalization or AI-assisted multispectral analysis. Beyond physical limitations, practical translation is further impeded by engineering and standardization challenges. In particular, device-to-device reproducibility, large scale nanofabrication, long-term measurement stability, and the absence of unified calibration and benchmarking protocols remain major barriers to industrial adoption. From a commercialization perspective, future progress will rely not only on further sensitivity enhancement, but also on the development of scalable, cost-effective, and reproducible nanophotonic platforms with standardized performance metrics. In this context, point-of-care testing[325] and lab-on-chip[326] integration offer promising pathways toward compact and automated detection, while hybrid multimodal strategies that couple optical, electrochemical[327], and mass-sensitive detection may improve robustness and accelerate the transition from laboratory demonstrations to application-ready chiral sensing systems.

Besides, artificial intelligence is emerging as a valuable complement to these advances, providing tools for extracting hidden spectral features, classifying molecular handedness, and enabling inverse design of photonic structures. Emerging frontiers now focus on enhancing autonomy, accessibility, and interpretability. Self-supervised learning alleviates the dependence on labelled datasets for identification of novel particles; edge computing integrates lightweight models like MobileNet into portable devices for real-time monitoring of environmental pollutants; and explainable AI methods like SHAP values provide interpretability, revealing how features contribute to classification outcomes and thereby building user trust. These advancements collectively position machine learning not merely as analytical tools but as discovery catalysts—bridging raw data complexity with scientific insight across materials science, environmental monitoring, and biomedical diagnostics. The combination of AI-driven analysis with engineered optical fields offers a promising pathway to achieve robust, high-throughput, and autonomous chiral sorting and sensing.

In summary, the convergence of photonic nanostructures, microfluidic integration, and intelligent data processing is expected to accelerate the transition from proof-of-concept demonstrations toward real-world applications. Such advances will be particularly impactful in pharmaceutical manufacturing, clinical diagnostics, and enantioselective catalysis, where precise control and reliable identification of chirality remain indispensable.

## References


1. Guijarro A, Yus M. *The Origin of Chirality in the Molecules of Life: A Revision from Awareness to the Current Theories and Perspectives of this Unsolved Problem* (The Royal Society of Chemistry, Cambridge, 2008).
2. Botta O, Bada JL, Gomez-Elvira J et al. *Strategies of Life Detection* (Springer, New York, 2008).
3. Kim JH, Scialli AR. Thalidomide: the tragedy of birth defects and the effective treatment of disease. *Toxicol Sci* **122**, 1–6 (2011).
4. Morvan M, Mikšík I. Recent advances in chiral analysis of proteins and peptides. *Separations* **8**, 112 (2021).
5. Wang ZY, Zhou Z, Zhang H et al. Vectorial liquid-crystal holography. *eLight* **4**, 5 (2024).
6. Chela-Flores J. The origin of chirality in protein amino acids. *Chirality* **6**, 165–168 (1994).
7. Agranat I, Caner H, Caldwell J. Putting chirality to work: the strategy of chiral switches. *Nat Rev Drug Discov* **1**, 753–768 (2002).
8. Nguyen LA, He H, Pham-Huy C. Chiral drugs: an overview. *Int J Biomed Sci* **2**, 85–100 (2006).
9. Zerrouki D, Baudry J, Pine D et al. Chiral colloidal clusters. *Nature* **455**, 380–382 (2008).
10. Brenna E, Fuganti C, Serra S. Enantioselective perception of chiral odorants. *Tetrah: Asymm* **14**, 1–42 (2003).
11. Zhang YQ, Cheng LC, Zhao FJ et al. Chiral pesticides selectively influence the dissemination of antibiotic resistance genes: an overlooked environmental risk. *Environ Sci Technol* **59**, 13374–13384 (2025).
12. Ni HZ, Xu WT, Xu LN et al. Mercapto-*β*-cyclodextrin grafting uniform spherical covalent organic frameworks for enantioseparation in liquid chromatography. *Anal Chim Acta* **1363**, 344186 (2025).
13. Bhattacharjee P, Dvorácskó S, Pointeau O et al. Evaluation of tetrahydropyridazine-based peripherally restricted dual inhibitors of CB1R and inducible nitric oxide synthase (iNOS) for treating metabolic syndrome disorders. *Metabolism* **170**, 156291 (2025).
14. Lyu M, Li C, Liu YZ et al. A salt-driven mechanism for precise chirality sorting of carbon nanotubes. *Sci Adv* **11**, eadx3958 (2025).
15. Zhao DW, Sun JJ, Chen N et al. Catalytic asymmetric *P*-site dearomatization enables kinetic resolution. *J Am Chem Soc* **147**, 23202–23212 (2025).
16. Liu YR, Ding HR, Li JG et al. Light-driven single-cell rotational adhesion frequency assay. *eLight* **2**, 13 (2022).
17. Stoev ID, Seelbinder B, Erben E et al. Highly sensitive force measurements in an optically generated, harmonic hydrodynamic trap. *eLight* **1**, 7 (2021).
18. Warning LA, Miandashti AR, McCarthy LA et al. Nanophotonic approaches for chirality sensing. *ACS Nano* **15**, 15538–15566 (2021).
19. Mun J, Kim M, Yang Y et al. Electromagnetic chirality: from fundamentals to nontraditional chiroptical phenomena. *Light Sci Appl* **9**, 139 (2020).
20. Solomon ML, Saleh AAE, Poulikakos LV et al. Nanophotonic platforms for chiral sensing and separation. *Acc Chem Res* **53**, 588–598 (2020).
21. Kuznetsov AI, Brongersma ML, Yao J et al. Roadmap for optical metasurfaces. *ACS Photonics* **11**, 816–865 (2024).
22. Schulz SA, Oulton RF, Kenney M et al. Roadmap on photonic metasurfaces. *Appl Phys Lett* **124**, 260701 (2024).
23. Yin SX, Galiffi E, Alù A. Floquet metamaterials. *eLight* **2**, 8 (2022).
24. Liu XJ, Gu MN, Tian Y et al. Research progress on generating perfect vortex beams based on metasurfaces. *Opto-Electron Sci* **4**, 250007 (2025).
25. Zhu JM, Zhu XQ, Zuo YF et al. Optofluidics: the interaction between light and flowing liquids in integrated devices. *Opto-Electron Adv* **2**, 190007 (2019).
26. Minopoli A, Wagner S, Erben E et al. ISO-FLUCS: symmetrization

of optofluidic manipulations in quasi-isothermal micro-environments. *eLight* **3**, 16 (2023).
27. Kang M, Liu T, Chan CT et al. Applications of bound states in the continuum in photonics. *Nat Rev Phys* **5**, 659–678 (2023).
28. Li AD, Wei H, Cotrufo M et al. Exceptional points and non-Hermitian photonics at the nanoscale. *Nat Nanotechnol* **18**, 706–720 (2023).
29. Lee H, Kecebas A, Wang FF et al. Chiral exceptional point and coherent suppression of backscattering in silicon microring with low loss Mie scatterer. *eLight* **3**, 20 (2023).
30. Savinov V, Fedotov VA, Zheludev NI. Toroidal dipolar excitation and macroscopic electromagnetic properties of metamaterials. *Phys Rev B* **89**, 205112 (2014).
31. Ahmadivand A, Gerislioglu B, Ahuja R et al. Toroidal metaphotonics and metadevices. *Laser Photonics Rev* **14**, 1900326 (2020).
32. Tong JC, Suo F, Ma JHZ et al. Surface plasmon enhanced infrared photodetection. *Opto-Electron Adv* **2**, 180026 (2019).
33. Ma H, Pan SQ, Wang WL et al. Surface-enhanced Raman spectroscopy: current understanding, challenges, and opportunities. *ACS Nano* **18**, 14000–14019 (2024).
34. Wu NF, Sun YX, Hu JT et al. Intelligent nanophotonics: when machine learning sheds light. *eLight* **5**, 5 (2025).
35. Krasikov S, Tranter A, Bogdanov A et al. Intelligent metaphotonics empowered by machine learning. *Opto-Electron Adv* **5**, 210147 (2022).
36. Tkachenko G, Brasselet E. Spin controlled optical radiation pressure. *Phys Rev Lett* **111**, 033605 (2013).
37. Tkachenko G, Brasselet E. Helicity-dependent three-dimensional optical trapping of chiral microparticles. *Nat Commun* **5**, 4491 (2014).
38. Wang SB, Chan CT. Lateral optical force on chiral particles near a surface. *Nat Commun* **5**, 3307 (2014).
39. Kravets N, Aleksanyan A, Brasselet E. Chiral optical Stern-Gerlach newtonian experiment. *Phys Rev Lett* **122**, 024301 (2019).
40. Brzobohatý O, Karásek V, Šiler M et al. Experimental demonstration of optical transport, sorting and self-arrangement using a 'tractor beam'. *Nat Photonics* **7**, 123–127 (2013).
41. Ali R, Dutra RS, Pinheiro FA et al. Enantioselection and chiral sorting of single microspheres using optical pulling forces. *Opt Lett* **46**, 1640–1643 (2021).
42. Li MM, Yan SH, Zhang YN et al. Optical sorting of small chiral particles by tightly focused vector beams. *Phys Rev A* **99**, 033825 (2019).
43. Fang L, Wang J. Optical trapping separation of chiral nanoparticles by subwavelength slot waveguides. *Phys Rev Lett* **127**, 233902 (2021).
44. Mao LB, Cheng PY, Liu K et al. Sieving nanometer enantiomers using bound states in the continuum from the metasurface. *Nanoscale Adv* **4**, 1617–1625 (2022).
45. Zhang JY, He T, Li CF et al. High-speed sorting of sub-20 nm chiral particles via toroidal-enhanced separated potential wells. *Nano Lett* **25**, 6539–6547 (2025).
46. Gal J. Pasteur and the art of chirality. *Nat Chem* **9**, 604–605 (2017).
47. Schaaff TG, Whetten RL. Giant gold-glutathione cluster compounds: intense optical activity in metal-based transitions. *J Phys Chem B* **104**, 2630–2641 (2000).
48. Hendry E, Carpy T, Johnston J et al. Ultrasensitive detection and characterization of biomolecules using superchiral fields. *Nat Nanotechnol* **5**, 783–787 (2010).
49. Tang YQ, Cohen AE. Enhanced enantioselectivity in excitation of chiral molecules by superchiral light. *Science* **332**, 333–336 (2011).
50. Yoo S, Park QH. Chiral light-matter interaction in optical resonators. *Phys Rev Lett* **114**, 203003 (2015).
51. Jeong HH, Mark AG, Fischer P. Magnesium plasmonics for UV applications and chiral sensing. *Chem Commun* **52**, 12179–12182 (2016).
52. Zhang YC, Liu JQ, Li D et al. Self-assembled core–satellite gold nanoparticle networks for ultrasensitive detection of chiral molecules by recognition tunneling current. *ACS Nano* **10**, 5096–5103 (2016).
53. Solomon ML, Hu J, Lawrence M et al. Enantiospecific optical enhancement of chiral sensing and separation with dielectric metasurfaces. *ACS Photonics* **6**, 43–49 (2019).
54. Wu XW, Han X, Xu QS et al. Chiral BINOL-based covalent organic frameworks for enantioselective sensing. *J Am Chem Soc* **141**, 7081–7089 (2019).
55. De los Santos ZA, MacAvaney S, Russell K et al. Tandem use of optical sensing and machine learning for the determination of absolute configuration, enantiomeric and diastereomeric ratios, and concentration of chiral samples. *Angew Chem Int Ed* **59**, 2440–2448 (2020).
56. Chen Y, Zhao C, Zhang YZ et al. Integrated molar chiral sensing based on high-*Q* metasurface. *Nano Lett* **20**, 8696–8703 (2020).
57. Wang GY, Hao CL, Ma W et al. Chiral plasmonic triangular nanorings with SERS activity for ultrasensitive detection of amyloid proteins in Alzheimer's disease. *Adv Mater* **33**, 2102337 (2021).
58. Wu YT, Tang MQ, Barsoum ML et al. Functional crystalline porous framework materials based on supramolecular macrocycles. *Chem Soc Rev* **54**, 2906–2947 (2025).
59. Almohammadi H, Khadem SA, Azzari P et al. Liquid–liquid crystalline phase separation of filamentous colloids and semiflexible polymers: experiments, theory and simulations. *Rep Prog Phys* **88**, 036601 (2025).
60. Kang X, Yu MY, Xu Y et al. Nanochannel functionalization using POFs: progress and prospects. *Adv Colloid Interface Sci* **342**, 103533 (2025).
61. Bloom BP, Paltiel Y, Naaman R et al. Chiral induced spin selectivity. *Chem Rev* **124**, 1950–1991 (2024).
62. Yu YB, Hu YN, Ning CB et al. BINOL-based chiral macrocycles and cages. *Angew Chem Int Ed* **63**, e202407034 (2024).
63. Vijayakanth T, Dasgupta S, Ganatra P et al. Peptide hydrogen-bonded organic frameworks. *Chem Soc Rev* **53**, 3640–3655 (2024).
64. Cheng QS, Ma Q, Pei HB et al. Enantioseparation membranes: research status, challenges, and trends. *Small* **19**, 2300376 (2023).
65. Liu GF, Humphrey MG, Zhang C et al. Self-assembled stereomutation with supramolecular chirality inversion. *Chem Soc Rev* **52**, 4443–4487 (2023).
66. Sui JC, Wang N, Wang JK et al. Strategies for chiral separation: from racemate to enantiomer. *Chem Sci* **14**, 11955–12003 (2023).
67. Barman K, Islam M, Das S et al. Recent advances in enantiorecognition and enantioseparation techniques of chiral molecules in the pharmaceutical field. *Biomed Chromatogr* **39**, e6073 (2025).
68. Zhu GG, Ge L, Li XY et al. Development and application of chiral separation technology based on chiral metal-organic frameworks. *J Pharm Anal* **15**, 101176 (2025).
69. Niu XH, Liu YQ, Zhao R et al. Mechanisms for translating chiral enantiomers separation research into macroscopic visualization. *Adv Colloid Interface Sci* **335**, 103342 (2025).
70. Liu YR, Wu ZL, Armstrong DW et al. Detection and analysis of chiral molecules as disease biomarkers. *Nat Rev Chem* **7**, 355–373 (2023).
71. Gao XY, Ben T. Chiral substrate-induced chiral covalent organic framework membranes for enantioselective separation of macromolecular drug. *Nat Commun* **16**, 5210 (2025).
72. Zhang XF, Hou B, Li ZP et al. Highly enantioselective transportation across liquid membranes mediated by porous covalent organic

frameworks. *Angew Chem Int Ed* **64**, e202419916 (2025).
73. Chen T, Li H, Shi XS et al. Robust homochiral polycrystalline metal-organic framework membranes for high-performance enantioselective separation. *J Am Chem Soc* **146**, 14433–14438 (2024).
74. Manoranjan N, Fang WX, Zhu YZ et al. A chiral COFs membrane for enantioselective amino acid separation. *Angew Chem Int Ed* **64**, e202417088 (2025).
75. Guo J, Duan YL, Jia YL et al. Biomimetic chiral hydrogen-bonded organic-inorganic frameworks. *Nat Commun* **15**, 139 (2024).
76. Ge L, Zhu GG, Li XY et al. Triazole-amine metal-organic framework chiral stationary phases: a novel chiral separation approach for amino acids in capillary electrochromatography. *Anal Chim Acta* **1368**, 344340 (2025).
77. Horáček O, Nováková L, Tüzün E et al. Advanced tool for chiral separations of anionic and zwitterionic (metalla)carboranes: supercritical fluid chromatography. *Anal Chem* **94**, 17551–17558 (2022).
78. Xu JH, Zhang JY, Zhang WM et al. Controllable synthesis of chiral hierarchical porous $Co(OH)_2$ and its application in rapid chiral recognition and separation. *Anal Chim Acta* **1364**, 344212 (2025).
79. Yan XS, Cao JL, Luo H et al. Heterochiral coupling to bilateral β-turn structured azapeptides bearing two remote chiral centers. *Nat Commun* **15**, 9271 (2024).
80. Berreur J, Watts OFB, Bulless THN et al. Redox-powered autonomous directional C-C bond rotation under enzyme control. *Nature* **644**, 96–101 (2025).
81. Wang FMJ, He KQ, Wang RX et al. A homochiral porous organic cage-polymer membrane for enantioselective resolution. *Adv Mater* **36**, 2400709 (2024).
82. Wu Q, Liang J, Wang D et al. Host molecules inside metal-organic frameworks: host@MOF and guest@host@MOF (Matrjoschka) materials. *Chem Soc Rev* **54**, 601–622 (2025).
83. Fu SG, Qin GZ, Dong JQ et al. Construction of chiral crown ethers in robust covalent organic frameworks for electrochromatographic enantioseparation. *Natl Sci Rev* **11**, nwae256 (2024).
84. Wang XX, Xiang S, Qi CX et al. Visualization of enantiorecognition and resolution by chiral AIEgens. *ACS Nano* **16**, 8223–8232 (2022).
85. Jeon J, Giovane Kappenberg Y, Gautam AK et al. Planar chiral metallopolymers for electrochemically mediated enantioselective separations. *J Am Chem Soc* **147**, 17880–17889 (2025).
86. Chen C, Ma YL, Yao KD et al. Enantioselective adsorption on chiral ceramics with medium entropy. *Nat Commun* **15**, 10105 (2024).
87. Jang J, Coquerel G, Seo TS et al. Microfluidic antisolvent crystallization for chiral symmetry breaking. *Lab Chip* **24**, 5055–5064 (2024).
88. Mangelings D, Heyden YV. High-throughput screening and optimization approaches for chiral compounds by means of microfluidic devices. *Comb Chem High Throughput Screen* **10**, 317–325 (2007).
89. Li YK, Liu C, Bai X et al. Enantiomorphic microvortex-enabled supramolecular sensing of racemic amino acids by using achiral building blocks. *Angew Chem Int Ed* **59**, 3486–3490 (2020).
90. Marcos, Fu HC, Powers TR et al. Separation of microscale chiral objects by shear flow. *Phys Rev Lett* **102**, 158103 (2009).
91. Chen HX, Deng QP, Zhang LW et al. Quantification of testosterone and epitestosterone in biological samples by capillary electrophoresis with immunoaffinity extraction. *Talanta* **78**, 464–470 (2009).
92. Shi YZ, Zhu TT, Zhang TH et al. Chirality-assisted lateral momentum transfer for bidirectional enantioselective separation. *Light Sci Appl* **9**, 62 (2020).
93. Yokota M, He SL, Takenaka T. Scattering of a Hermite-Gaussian beam field by a chiral sphere. *J Opt Soc Am A* **18**, 1681–1689 (2001).
94. Zhou LM, Shi YZ, Zhu XY et al. Recent progress on optical micro/nanomanipulations: structured forces, structured particles, and synergetic applications. *ACS Nano* **16**, 13264–13278 (2022).
95. Chen HJ, Liang CH, Liu SY et al. Chirality sorting using two-wave-interference-induced lateral optical force. *Phys Rev A* **93**, 053833 (2016).
96. Zhang TH, Mahdy MRC, Liu YM et al. All-optical chirality-sensitive sorting *via* reversible lateral forces in interference fields. *ACS Nano* **11**, 4292–4300 (2017).
97. Ding K, Ng J, Zhou L et al. Realization of optical pulling forces using chirality. *Phys Rev A* **89**, 063825 (2014).
98. Nieto-Vesperinas M, Sáenz JJ, Gómez-Medina R et al. Optical forces on small magnetodielectric particles. *Opt Express* **18**, 11428–11443 (2010).
99. Chaumet PC, Rahmani A. Electromagnetic force and torque on magnetic and negative-index scatterers. *Opt Express* **17**, 2224–2234 (2009).
100. Shi HS, Zheng HX, Chen HJ et al. Optical binding and lateral forces on chiral particles in linearly polarized plane waves. *Phys Rev A* **101**, 043808 (2020).
101. Chen J, Ng J, Lin ZF et al. Optical pulling force. *Nat Photonics* **5**, 531–534 (2011).
102. Wen JQ, Chen HJ, Zheng HX et al. Optical intensity-gradient torque due to chiral multipole interplay. *Photonics Res* **13**, 2903–2912 (2025).
103. Xu XH, Nieto-Vesperinas M, Zhou Y et al. Gradient and curl optical torques. *Nat Commun* **15**, 6230 (2024).
104. He T, Zhang JY, Tsai DP et al. A review on optical torques: from engineered light fields to objects. *Opto-Electron Sci* **4**, 250014 (2025).
105. Zhou Y, Xu XH, Zhang YN et al. Observation of high-order imaginary Poynting momentum optomechanics in structured light. *Proc Natl Acad Sci USA* **119**, e2209721119 (2022).
106. Shi YZ, Xu XH, Nieto-Vesperinas M et al. Advances in light transverse momenta and optical lateral forces. *Adv Opt Photonics* **15**, 835–906 (2023).
107. Nshii CC, Vangeleyn M, Cotter JP et al. A surface-patterned chip as a strong source of ultracold atoms for quantum technologies. *Nat Nanotechnol* **8**, 321–324 (2013).
108. Zhu LX, Liu X, Sain B et al. A dielectric metasurface optical chip for the generation of cold atoms. *Sci Adv* **6**, eabb6667 (2020).
109. Ashkin A. Acceleration and trapping of particles by radiation pressure. *Phys Rev Lett* **24**, 156–159 (1970).
110. Tkachenko G, Brasselet E. Optofluidic sorting of material chirality by chiral light. *Nat Commun* **5**, 3577 (2014).
111. Donato MG, Hernandez J, Mazzulla A et al. Polarization-dependent optomechanics mediated by chiral microresonators. *Nat Commun* **5**, 3656 (2014).
112. Abujetas DR, Marqués MI, Sánchez-Gil JA. Modulated flipping torque, spin-induced radiation pressure, and chiral sorting exerted by guided light. *Opt Express* **29**, 16969–16979 (2021).
113. Yi WC, Huang HY, Lai CX et al. Optical forces on chiral particles: science and applications. *Micromachines* **15**, 1267 (2024).
114. Chu S, Bjorkholm JE, Ashkin A et al. Experimental observation of optically trapped atoms. *Phys Rev Lett* **57**, 314–317 (1986).
115. Zheng HX, Chen HJ, Ng J et al. Optical gradient force in the absence of light intensity gradient. *Phys Rev B* **103**, 035103 (2021).
116. Yamanishi J, Ahn HY, Yamane H et al. Optical gradient force on chiral particles. *Sci Adv* **8**, eabq2604 (2022).
117. Ali R, Pinheiro FA, Dutra RS et al. Enantioselective manipulation of single chiral nanoparticles using optical tweezers. *Nanoscale* **12**, 5031–5037 (2020).

118. Bradshaw DS, Forbes KA, Leeder JM et al. Chirality in optical trapping and optical binding. *Photonics* **2**, 483–497 (2015).
119. Bradshaw DS, Andrews DL. Chiral discrimination in optical trapping and manipulation. *New J Phys* **16**, 103021 (2014).
120. Brzobohatý O, Hernández RJ, Simpson S et al. Chiral particles in the dual-beam optical trap. *Opt Express* **24**, 26382–26391 (2016).
121. Zhu TT, Shi YZ, Ding WQ et al. Extraordinary multipole modes and ultra-enhanced optical lateral force by chirality. *Phys Rev Lett* **125**, 043901 (2020).
122. Chen HJ, Zheng HX, Lu WL et al. Lateral optical force due to the breaking of electric-magnetic symmetry. *Phys Rev Lett* **125**, 073901 (2020).
123. Sukhov S, Kajorndejnukul V, Naraghi RR et al. Dynamic consequences of optical spin-orbit interaction. *Nat Photonics* **9**, 809–812 (2015).
124. Rodríguez-Fortuño FJ, Engheta N, Martínez A et al. Lateral forces on circularly polarizable particles near a surface. *Nat Commun* **6**, 8799 (2015).
125. Zhang ZB, Min CJ, Fu YN et al. Controllable transport of nanoparticles along waveguides by spin-orbit coupling of light. *Opt Express* **29**, 6282–6292 (2021).
126. Zhang Q, Li JQ, Liu XG. Optical lateral forces and torques induced by chiral surface-plasmon-polaritons and their potential applications in recognition and separation of chiral enantiomers. *Phys Chem Chem Phys* **21**, 1308–1314 (2019).
127. Sukhov S, Dogariu A. Non-conservative optical forces. *Rep Prog Phys* **80**, 112001 (2017).
128. Quidant R, Girard C. Surface-plasmon-based optical manipulation. *Laser Photonics Rev* **2**, 47–57 (2008).
129. Lai CX, Shi YZ, Huang HY et al. Observation of intricate chiral optical force in a spin-curl light field. *Phys Rev Lett* **133**, 233802 (2024).
130. Lee SH, Roichman Y, Grier DG. Optical solenoid beams. *Opt Express* **18**, 6988–6993 (2010).
131. Novitsky A, Qiu CW, Wang HF. Single gradientless light beam drags particles as tractor beams. *Phys Rev Lett* **107**, 203601 (2011).
132. Sukhov S, Dogariu A. On the concept of “tractor beams”. *Opt Lett* **35**, 3847–3849 (2010).
133. Zheng HX, Li X, Chen HJ et al. Selective transport of chiral particles by optical pulling forces. *Opt Express* **29**, 42684–42695 (2021).
134. Li MM, Yan SH, Zhang YN et al. Optical separation and discrimination of chiral particles by vector beams with orbital angular momentum. *Nanoscale Adv* **3**, 6897–6902 (2021).
135. Zhang YN, Li MM, Yan SH et al. Identification and separation of chiral particles by focused circularly polarized vortex beams. *J Opt Soc Am A* **39**, 1371–1377 (2022).
136. Ali R, Pinheiro FA, Dutra RS et al. Enantioselective optical forces and size-dependent sorting of single chiral particles using vortex beams. *Phys Rev B* **110**, 115412 (2024).
137. Xiong X, Zhou YT, Lu S et al. Enantioselective optical trapping of chiral nanoparticles by tightly focused fractional vector beams. *Opt Express* **32**, 34639–34650 (2024).
138. Li MM, Yan SH, Zhang YN et al. Generation of controllable chiral optical fields by vector beams. *Nanoscale* **12**, 15453–15459 (2020).
139. Man ZS, Zhang YQ, Cai YJ et al. Construction of chirality-sorting optical force pairs. *Phys Rev Lett* **133**, 233803 (2024).
140. Li BJ. Chirality sorting using a structured caustic vector vortex field. *J Opt Soc Am B* **39**, 1676–1685 (2022).
141. Ying XY, Rui GH, Zou ST et al. Synthesis of multiple longitudinal polarization vortex structures and its application in sorting chiral nanoparticles. *Opt Express* **29**, 19001–19014 (2021).
142. Liu XG, Li JQ, Zhang Q et al. Separation of chiral enantiomers by optical force and torque induced by tightly focused vector polarized hollow beams. *Phys Chem Chem Phys* **21**, 15339–15345 (2019).
143. Wu H, Zhang P, Zhang XJ et al. Selective trapping of chiral nanoparticles via vector Lissajous beams. *Opt Express* **30**, 3592–3600 (2022).
144. Yao J, Bai YH, Liu YD et al. Sorting of enantiomers using optical chirality in uniform light field. *Appl Phys Lett* **124**, 191104 (2024).
145. Hayat A, Mueller JPB, Capasso F. Lateral chirality-sorting optical forces. *Proc Natl Acad Sci USA* **112**, 13190–13194 (2015).
146. Cao T, Tian L, Liang HW et al. Reconfigurable, graphene-coated, chalcogenide nanowires with a sub-10-nm enantioselective sorting capability. *Microsyst Nanoeng* **4**, 7 (2018).
147. Martínez-Romeu J, Diez I, Golat S et al. Chiral forces in longitudinally invariant dielectric photonic waveguides. *Photonics Res* **12**, 431 (2024).
148. Yang M, Shi YZ, Song QH et al. Optical sorting: past, present and future. *Light Sci Appl* **14**, 103 (2025).
149. Luo H, Fang X, Li CF et al. 1 nm-resolution sorting of sub-10 nm nanoparticles using a dielectric metasurface with toroidal responses. *Small Sci* **3**, 2300100 (2023).
150. Hong CC, Yang S, Ndukaife JC. Stand-off trapping and manipulation of sub-10 nm objects and biomolecules using opto-thermo-electrohydrodynamic tweezers. *Nat Nanotechnol* **15**, 908–913 (2020).
151. Cao T, Qiu YM. Lateral sorting of chiral nanoparticles using Fano-enhanced chiral force in visible region. *Nanoscale* **10**, 566–574 (2018).
152. Cao T, Mao LB, Qiu YM et al. Fano resonance in asymmetric plasmonic nanostructure: separation of sub-10 nm enantiomers. *Adv Opt Mater* **7**, 1801172 (2019).
153. Safkat K, Rahim M, Mahdy MRC. Optical sorting of a plasmonic or dielectric or chiral mie object using a single metasurface. *Ann Phys* **534**, 2100402 (2022).
154. Tang X, Kuai Y, Fan ZT et al. Achiral and chiral optical force within topological optical lattices generated with plasmonic metasurfaces and tunable incident beam. *Phys Rev Appl* **19**, 054016 (2023).
155. Wang JT, Tonkaev P, Koshelev K et al. Resonantly enhanced second- and third-harmonic generation in dielectric nonlinear metasurfaces. *Opto-Electron Adv* **7**, 230186 (2024).
156. Feng ZW, Shi T, Geng GZ et al. Dual-band polarized upconversion photoluminescence enhanced by resonant dielectric metasurfaces. *eLight* **3**, 21 (2023).
157. Fan JX, Li ZL, Xue ZQ et al. Hybrid bound states in the continuum in terahertz metasurfaces. *Opto-Electron Sci* **2**, 230006 (2023).
158. Yao J, Lai FX, Fan YB et al. Nonlocal meta-lens with Huygens’ bound states in the continuum. *Nat Commun* **15**, 6543 (2024).
159. Chen Y, Deng HC, Sha XB et al. Observation of intrinsic chiral bound states in the continuum. *Nature* **613**, 474–478 (2023).
160. Qin HY, Su ZP, Zhang Z et al. Disorder-assisted real-momentum topological photonic crystal. *Nature* **639**, 602–608 (2025).
161. Zeng YX, Sha XB, Zhang C et al. Metalasers with arbitrarily shaped wavefront. *Nature* **643**, 1240–1245 (2025).
162. Liang Y, Tsai DP, Kivshar Y. From local to nonlocal high-*Q* plasmonic metasurfaces. *Phys Rev Lett* **133**, 053801 (2024).
163. Koshelev K, Kruk S, Melik-Gaykazyan E et al. Subwavelength dielectric resonators for nonlinear nanophotonics. *Science* **367**, 288–292 (2020).
164. Zhang F, Solodovchenko NS, Fan HK et al. Non-Hermitian singularities in scattering spectra of Mie resonators. *Sci Adv* **11**, eadr9183 (2025).
165. He T, Zhang ZY, Zhu JY et al. Scattering exceptional point in the visible. *Light Sci Appl* **12**, 229 (2023).

166. Yang ZJ, Huang PS, Lin YT et al. Creating pairs of exceptional points for arbitrary polarization control: asymmetric vectorial wavefront modulation. *Nat Commun* **15**, 232 (2024).
167. Song QH, Odeh M, Zúñiga-Pérez J et al. Plasmonic topological metasurface by encircling an exceptional point. *Science* **373**, 1133–1137 (2021).
168. Chen WJ, Kaya Özdemir Ş, Zhao GM et al. Exceptional points enhance sensing in an optical microcavity. *Nature* **548**, 192–196 (2017).
169. Hodaei H, Hassan AU, Wittek S et al. Enhanced sensitivity at higher-order exceptional points. *Nature* **548**, 187–191 (2017).
170. Park JH, Ndao A, Cai W et al. Symmetry-breaking-induced plasmonic exceptional points and nanoscale sensing. *Nat Phys* **16**, 462–468 (2020).
171. Wiersig J. Review of exceptional point-based sensors. *Photonics Res* **8**, 1457–1467 (2020).
172. Yi C, Wang ZJ, Shi YY et al. Creating topological exceptional point by on-chip all-dielectric metasurface. *Light Sci Appl* **14**, 262 (2025).
173. Mao LB, Liu K, Lian M et al. Bound states in the continuum in all-dielectric metasurface: separation of sub-10 nm enantiomers. *Adv Photonics Res* **3**, 2100280 (2022).
174. Liu N, Wang ST, Lv JT et al. Achiral nanoparticle trapping and chiral nanoparticle separating with quasi-BIC metasurface. *Opt Express* **31**, 28912–28928 (2023).
175. Jin RC, Zhang XZ, Huo PC et al. Harnessing enantioselective optical forces by quasibound states in the continuum. *Phys Rev Lett* **133**, 086901 (2024).
176. Li Z, Chen JX, Li LZ et al. Exceptional-point-enhanced sensing in an all-fiber bending sensor. *Opto-Electron Adv* **6**, 230019 (2023).
177. Kim C, Lu XD, Kong DM et al. Parity-time symmetry enabled ultra-efficient nonlinear optical signal processing. *eLight* **4**, 6 (2024).
178. Zhang CZ, Cheng YQ, Wang SB. Enhanced optical forces on coupled chiral particles at arbitrary order exceptional points. *Opt Express* **31**, 28929–28938 (2023).
179. Liu Y, Zhang WX, He L et al. All-optical separation of chiral nanoparticles on silicon-based microfluidic chips with vector exceptional points. *APL Photonics* **8**, 036112 (2023).
180. Doi M, Makino M. Separation of chiral particles in a rotating electric field. *Phys Fluids* **28**, 093302 (2016).
181. Banerjee-Ghosh K, Ben Dor O, Tassinari F et al. Separation of enantiomers by their enantiospecific interaction with achiral magnetic substrates. *Science* **360**, 1331–1334 (2018).
182. McNeill JM, Choi YC, Cai YY et al. Three-dimensionally complex phase behavior and collective phenomena in mixtures of acoustically powered chiral microspinners. *ACS Nano* **17**, 7911–7919 (2023).
183. Zhou Y, Yoon J. Recent progress in fluorescent and colorimetric chemosensors for detection of amino acids. *Chem Soc Rev* **41**, 52–67 (2012).
184. Gu LQ, Shim JW. Single molecule sensing by nanopores and nanopore devices. *Analyst* **135**, 441–451 (2010).
185. Ilisz I, Berkecz R, Péter A. Application of chiral derivatizing agents in the high-performance liquid chromatographic separation of amino acid enantiomers: a review. *J Pharm Biomed Anal* **47**, 1–15 (2008).
186. Blaschke G, Chankvetadze B. Enantiomer separation of drugs by capillary electromigration techniques. *J Chromatogr A* **875**, 3–25 (2000).
187. Beccaria M, Cabooter D. Current developments in LC-MS for pharmaceutical analysis. *Analyst* **145**, 1129–1157 (2020).
188. Tiwari MP, Prasad A. Molecularly imprinted polymer based enantioselective sensing devices: a review. *Anal Chim Acta* **853**, 1–18 (2015).
189. Preinerstorfer B, Lämmerhofer M, Lindner W. Advances in enantioselective separations using electromigration capillary techniques. *Electrophoresis* **30**, 100–132 (2009).
190. Schug KA, Lindner W. Chiral molecular recognition for the detection and analysis of enantiomers by mass spectrometric methods. *J Sep Sci* **28**, 1932–1955 (2005).
191. Liu J, Zhou H, Yang WR et al. Soft nanoarchitectonics for enantioselective biosensing. *Acc Chem Res* **53**, 644–653 (2020).
192. Han JM, Guo S, Lu H et al. Recent progress on circularly polarized luminescent materials for organic optoelectronic devices. *Adv Opt Mater* **6**, 1800538 (2018).
193. Mándi A, Kurtán T. Applications of OR/ECD/VCD to the structure elucidation of natural products. *Nat Prod Rep* **36**, 889–918 (2019).
194. Xu C, Ren ZH, Zhou H et al. Expanding chiral metamaterials for retrieving fingerprints via vibrational circular dichroism. *Light Sci Appl* **12**, 154 (2023).
195. Kuhar N, Sil S, Umapathy S. Potential of Raman spectroscopic techniques to study proteins. *Spectrochim Acta Part A Mol Biomol Spectrosc* **258**, 119712 (2021).
196. Böwering N, Lischke T, Schmidtke B et al. Asymmetry in photoelectron emission from chiral molecules induced by circularly polarized light. *Phys Rev Lett* **86**, 1187–1190 (2001).
197. Rouxel JR, Mukamel S. Molecular chirality and its monitoring by ultrafast X-ray pulses. *Chem Rev* **122**, 16802–16838 (2022).
198. Lipkin DM. Existence of a new conservation law in electromagnetic theory. *J Math Phys* **5**, 696–700 (1964).
199. Bliokh KY, Nori F. Characterizing optical chirality. *Phys Rev A* **83**, 021803 (2011).
200. Tang YQ, Cohen AE. Optical chirality and its interaction with matter. *Phys Rev Lett* **104**, 163901 (2010).
201. Shao MR, Ji C, Tan JB et al. Ferroelectrically modulate the Fermi level of graphene oxide to enhance SERS response. *Opto-Electron Adv* **6**, 230094 (2023).
202. Dong SL, He D, Zhang Q et al. Early cancer detection by serum biomolecular fingerprinting spectroscopy with machine learning. *eLight* **3**, 17 (2023).
203. Funck T, Nicoli F, Kuzyk A et al. Sensing picomolar concentrations of RNA using switchable plasmonic chirality. *Angew Chem Int Ed* **57**, 13495–13498 (2018).
204. Fang WN, Jia SS, Chao J et al. Quantizing single-molecule surface-enhanced Raman scattering with DNA origami metamolecules. *Sci Adv* **5**, eaau4506 (2019).
205. Zhou C, Xin L, Duan XY et al. Dynamic plasmonic system that responds to thermal and aptamer-target regulations. *Nano Lett* **18**, 7395–7399 (2018).
206. Halley PD, Patton RA, Chowdhury A et al. Low-cost, simple, and scalable self-assembly of DNA origami nanostructures. *Nano Res* **12**, 1207–1215 (2019).
207. Wang PF, Meyer TA, Pan V et al. The beauty and utility of DNA origami. *Chem* **2**, 359–382 (2017).
208. Rodier M, Keijzer C, Milner J et al. Biomacromolecular charge chirality detected using chiral plasmonic nanostructures. *Nanoscale Horiz* **5**, 336–344 (2020).
209. Zhang C, Hu HT, Ma CM et al. Quantum plasmonics pushes chiral sensing limit to single molecules: a paradigm for chiral biodetections. *Nat Commun* **15**, 2 (2024).
210. Kim RM, Han JH, Lee SM et al. Chiral plasmonic sensing: from the perspective of light-matter interaction. *J Chem Phys* **160**, 061001 (2024).
211. Hentschel M, Schäferling M, Duan XY et al. Chiral plasmonics. *Sci Adv* **3**, e1602735 (2017).
212. Bochenkov VE, Shabatina TI. Chiral plasmonic biosensors. *Biosensors* **8**, 120 (2018).
213. Zhou C, Duan XY, Liu N. DNA-nanotechnology-enabled chiral plasmonics: from static to dynamic. *Acc Chem Res* **50**, 2906–2914

(2017).
214. Neubrech F, Hentschel M, Liu N. Reconfigurable plasmonic chirality: fundamentals and applications. *Adv Mater* **32**, 1905640 (2020).
215. Ghamari S, Wu HY, Pedireddy S et al. Plasmonic nanorod and dimer chiral molecule sensing from cysteine monolayer to bi-layers and multilayered shells. *npj Biosens* **2**, 17 (2025).
216. Xi PY, Zhao WJ, Cao Y et al. Facile construction of soft plasmonic sensors with exceptional optical activity for quantitative chiral detection. *Small* **21**, 2408176 (2025).
217. Yang X, Huang SS, Chikkaraddy R et al. Chiral plasmonic shells: high-performance metamaterials for sensitive chiral biomolecule detection. *ACS Appl Mater Interfaces* **14**, 53183–53192 (2022).
218. Du W, Wen XL, Gérard D et al. Chiral plasmonics and enhanced chiral light-matter interactions. *Sci China Phys, Mech Astron* **63**, 244201 (2020).
219. Thapa DK, Biswas S. Chiral and quantum plasmonic sensors: new frontiers in selective and ultra-sensitive sensing. *Small* **21**, 2409197 (2025).
220. Lee YY, Kim RM, Im SW et al. Plasmonic metamaterials for chiral sensing applications. *Nanoscale* **12**, 58–66 (2020).
221. Rane S, Prabhu S, Chowdhury DR. Physics and applications of terahertz metagratings. *Opto-Electron Sci* **3**, 230049 (2024).
222. Kim J, Kim W, Oh DK et al. One-step printable platform for high-efficiency metasurfaces down to the deep-ultraviolet region. *Light Sci Appl* **12**, 68 (2023).
223. Yu ZP, Gao XY, Yao J et al. A spatial-frequency patching metasurface enabling super-capacity perfect vector vortex beams. *eLight* **4**, 21 (2024).
224. Fu R, Chen KX, Li ZL et al. Metasurface-based nanoprinting: principle, design and advances. *Opto-Electron Sci* **1**, 220011 (2022).
225. Chen YQ, Hu YQ, Zhao JY et al. Topology optimization-based inverse design of plasmonic nanodimer with maximum near-field enhancement. *Adv Funct Mater* **30**, 2000642 (2020).
226. Zhu ZB, Li YF, Wang JF et al. Reconfigurable origami chiral response for holographic imaging and information encryption. *Opto-Electron Sci* **4**, 240026 (2025).
227. Leng BR, Zhang Y, Tsai DP et al. Meta-device: advanced manufacturing. *Light Adv. Manuf* **5**, 5 (2024).
228. Park JS, Lim SWD, Amirzhan A et al. All-glass 100 mm diameter visible metalens for imaging the cosmos. *ACS Nano* **18**, 3187–3198 (2024).
229. Dorrah AH, Park JS, Palmieri A et al. Free-standing bilayer metasurfaces in the visible. *Nat Commun* **16**, 3126 (2025).
230. Zhang Y, Jiang X, Qu GY et al. On-chip integration of achromatic metalens arrays. *Nat Commun* **16**, 7485 (2025).
231. Rosas S, Adi W, Beisenova A et al. Enhanced biochemical sensing with high-*Q* transmission resonances in free-standing membrane metasurfaces. *Optica* **12**, 178–189 (2025).
232. Stav T, Faerman A, Maguid E et al. Quantum entanglement of the spin and orbital angular momentum of photons using metamaterials. *Science* **361**, 1101–1104 (2018).
233. Li L, Liu ZX, Ren XF et al. Metalens-array-based high-dimensional and multiphoton quantum source. *Science* **368**, 1487–1490 (2020).
234. Zhao Y, Askarpour AN, Sun LY et al. Chirality detection of enantiomers using twisted optical metamaterials. *Nat Commun* **8**, 14180 (2017).
235. Lin CY, Liu CC, Chen YY et al. Molecular chirality detection with periodic arrays of three-dimensional twisted metamaterials. *ACS Appl Mater Interfaces* **13**, 1152–1157 (2021).
236. Li HY, Ye WX, Polavarapu L et al. Chiral plasmonic superlattice resonance based on metasurfaces for chiral molecular sensors. *Opt Lett* **50**, 2900–2903 (2025).
237. Palermo G, Rippa M, Aceti DM et al. Intrinsic superchirality in planar plasmonic metasurfaces. *Nano Lett* **24**, 10202–10209 (2024).
238. Biswas A, Cencillo-Abad P, Shabbir MW et al. Tunable plasmonic superchiral light for ultrasensitive detection of chiral molecules. *Sci Adv* **10**, eadk2560 (2024).
239. Biswas A, Cencillo-Abad P, Chanda D. Multispectral molecular chiral barcoding. *Adv Mater* **36**, 2409565 (2024).
240. Indukuri SRKC, Frydendahl C, Sharma N et al. Enhanced chiral sensing at the few-molecule level using negative index metamaterial plasmonic nanocuvettes. *ACS Nano* **16**, 17289–17297 (2022).
241. Deng QM, Li X, Hu MX et al. Advances on broadband and resonant chiral metasurfaces. *npj Nanophoton* **1**, 20 (2024).
242. Yoo S, Park QH. Metamaterials and chiral sensing: a review of fundamentals and applications. *Nanophotonics* **8**, 249–261 (2019).
243. Wang ZY, Ai B, Zhou ZW et al. Free-standing plasmonic chiral metamaterials with 3D resonance cavities. *ACS Nano* **12**, 10914–10923 (2018).
244. Li CF, He T, Yang X et al. Enhanced circular dichroism for achiral sensing based on a DNA-origami-empowered anapole metasurface. *Nano Lett* **24**, 9451–9458 (2024).
245. Lee KT, Kim B, Raju L et al. Enantiomer-selective molecular sensing in the nonlinear optical regime via upconverting chiral metamaterials. *Adv Funct Mater* **32**, 2208641 (2022).
246. Manoccio M, Esposito M, Primiceri E et al. Femtomolar biodetection by a compact core-shell 3D chiral metamaterial. *Nano Lett* **21**, 6179–6187 (2021).
247. He HL, Cen MJ, Wang JW et al. Plasmonic chiral metasurface-induced upconverted circularly polarized luminescence from achiral upconversion nanoparticles. *ACS Appl Mater Interfaces* **14**, 53981–53989 (2022).
248. Gwak J, Nguyen HQ, Jeong KJ et al. Reconfigurable metasurface of magnetoplasmonic microbundle array for chiral signal enhancing. *Adv Opt Mater* **11**, 2202104 (2023).
249. Tseng ML, Lin ZH, Kuo HY et al. Stress-induced 3D chiral fractal metasurface for enhanced and stabilized broadband near-field optical chirality. *Adv Opt Mater* **7**, 1900617 (2019).
250. Chen C, Gao SL, Song WG et al. Metasurfaces with planar chiral meta-atoms for spin light manipulation. *Nano Lett* **21**, 1815–1821 (2021).
251. Probst PT, Mayer M, Gupta V et al. Mechano-tunable chiral metasurfaces via colloidal assembly. *Nat Mater* **20**, 1024–1028 (2021).
252. Liu WL, Han H, Wang JQ. Recent advances in the 3D chiral plasmonic nanomaterials. *Small* **20**, 2305725 (2024).
253. Cen MJ, Wang JW, Liu JX et al. Ultrathin suspended chiral metasurfaces for enantiodiscrimination. *Adv Mater* **34**, 2203956 (2022).
254. Asefa SA, Seong M, Lee D. Design of bilayer crescent chiral metasurfaces for enhanced chiroptical response. *Sensors* **25**, 915 (2025).
255. Lv SY, Zhang LL, Luo WF et al. Design and sensing performance study of chiral metasurfaces based on Bragg reflector. *Phys Lett A* **558**, 130877 (2025).
256. Gromyko D, An S, Gorelik S et al. Unidirectional chiral emission via twisted bi-layer metasurfaces. *Nat Commun* **15**, 9804 (2024).
257. Ni JC, Liu SL, Wu D et al. Gigantic vortical differential scattering as a monochromatic probe for multiscale chiral structures. *Proc Natl Acad Sci USA* **118**, e2020055118 (2021).
258. Kim AS, Goswami A, Taghinejad M et al. Phototransformation of achiral metasurfaces into handedness-selectable transient chiral media. *Proc Natl Acad Sci USA* **121**, e2318713121 (2024).
259. Chen WJ, Wang ZY, Gorkunov MV et al. Uncovering maximum chirality in resonant nanostructures. *Nano Lett* **24**, 9643–9649 (2024).
260. Zhang JC, Chen MK, Liang Y et al. Nanoimprint meta-device for chiral imaging. *Adv Funct Mater* **33**, 2306422 (2023).
261. Chen MK, Zhang JC, Leung CW et al. Chiral-magic angle of

nanoimprint meta-device. *Nanophotonics* **12**, 2479–2490 (2023).
262. Mohammadi E, Tavakoli A, Dehkhoda P et al. Accessible superchiral near-fields driven by tailored electric and magnetic resonances in all-dielectric nanostructures. *ACS Photonics* **6**, 1939–1946 (2019).
263. Mohammadi E, Tittl A, Tsakmakidis KL et al. Dual nanoresonators for ultrasensitive chiral detection. *ACS Photonics* **8**, 1754–1762 (2021).
264. Ye LF, Li JY, Richter FU et al. Dielectric tetramer nanoresonators supporting strong superchiral fields for vibrational circular dichroism spectroscopy. *ACS Photonics* **10**, 4377–4384 (2023).
265. Droulias S, Bougas L. Absolute chiral sensing in dielectric metasurfaces using signal reversals. *Nano Lett* **20**, 5960–5966 (2020).
266. Zhang XZ, Wang CT, Jin RC et al. Enhancing superchiral fields and circular dichroism detection with achiral dielectric metasurfaces. *Nano Lett* **25**, 12620–12626 (2025).
267. Leite TR, Zschiedrich L, Kizilkaya O et al. Resonant plasmonic-biomolecular chiral interactions in the far-ultraviolet: enantiomeric discrimination of sub-10 nm amino acid films. *Nano Lett* **22**, 7343–7350 (2022).
268. García-Guirado J, Svedendahl M, Puigdollers J et al. Enantiomer-selective molecular sensing using racemic nanoplasmonic arrays. *Nano Lett* **18**, 6279–6285 (2018).
269. Mohammadi E, Raziman TV, Curto AG. Nanophotonic chirality transfer to dielectric mie resonators. *Nano Lett* **23**, 3978–3984 (2023).
270. Li CF, He T, Rao XF et al. Toroidal dipole Fabry-Perot bound states in the continuum metasurfaces for ultrasensitive chiral detection. *Photonics Res* **13**, 2497–2509 (2025).
271. Guan TT, Wang ZY, Wang RZ et al. Ultrasensitive circular dichroism spectroscopy based on coupled quasi-bound states in the continuum. *Nanophotonics* **14**, 1083–1089 (2025).
272. Tang YH, Liang Y, Yao J et al. Chiral bound states in the continuum in plasmonic metasurfaces. *Laser Photonics Rev* **17**, 2200597 (2023).
273. Chen Y, Chen WJ, Kong XH et al. Can weak chirality induce strong coupling between resonant states. *Phys Rev Lett* **128**, 146102 (2022).
274. Huang SS, Wang SY, Yang X et al. Ultrasensitive ultraviolet chiral plasmonic biosensor based on passivated Al shells. *ACS Appl Mater Interfaces* **17**, 28532–28540 (2025).
275. Xu JH, Dong ZG, Asbahi M et al. Multiphoton upconversion enhanced by deep subwavelength near-field confinement. *Nano Lett* **21**, 3044–3051 (2021).
276. Wang Y, Zhao XQ, Yu Z et al. A chiral-label-free SERS strategy for the synchronous chiral discrimination and identification of small aromatic molecules. *Angew Chem Int Ed* **59**, 19079–19086 (2020).
277. Arabi M, Ostovan A, Wang YQ et al. Chiral molecular imprinting-based SERS detection strategy for absolute enantiomeric discrimination. *Nat Commun* **13**, 5757 (2022).
278. Leong SX, Koh CSL, Sim HYF et al. Enantiospecific molecular fingerprinting using potential-modulated surface-enhanced raman scattering to achieve label-free chiral differentiation. *ACS Nano* **15**, 1817–1825 (2021).
279. Dai QS, Huang JR, Qiu X et al. A chiral sensing system based on single Au nanowire: a general SERS strategy for identification of the enantiomers and mechanism for chiral interaction. *Anal Chem* **97**, 3765–3772 (2025).
280. Xu J, Xue YF, Jian XX et al. Understanding of chiral site-dependent enantioselective identification on a plasmon-free semiconductor based SERS substrate. *Chem Sci* **13**, 6550–6557 (2022).
281. Huang XQ, Chen QX, Ma YL et al. Chiral Au nanostars for SERS sensing of enantiomers discrimination, multibacteria recognition and photothermal antibacterial application. *Chem Eng J* **479**, 147528 (2024).
282. Abbas A, Zhang Q, Kazmi J et al. Label-free SERS fingerprinting for chiral discrimination using chiral two-dimensional superlattice. *Nano Lett* **25**, 12676–12684 (2025).
283. Xu J, Jian XX, Guo JL et al. Selective SERS identification and quantification of glucose enantiomers on homochiral MOFs based enzyme-free nanoreactors. *Chem Eng J* **459**, 141650 (2023).
284. Yadav S, Bhardwaj L, Singh JP. Ultrasensitive plasmonic chiral SERS substrate for ligand-free enantioselective discrimination and molecular fingerprinting. *ACS Appl Mater Interfaces* **17**, 46383–46395 (2025).
285. Pan SF, Tian XD, Lu Y et al. Wearable SERS-microfluidic patch for real-time in situ monitoring of chiral metabolites in sweat. *Small* **21**, 2500770 (2025).
286. Ma FY, Dou HM, Luo DN et al. Recent advances in chiral recognition based on surface-enhanced Raman scattering spectroscopy. *Chin Chem Lett* **37**, 111632 (2026).
287. Wang N, Zhao LJ, Liu C et al. Chiral detection of glucose: an amino acid-assisted surface-enhanced Raman scattering strategy showing opposite enantiomeric effects on SERS signals. *Anal Chem* **94**, 14565–14572 (2022).
288. Guselnikova O, Elashnikov R, Svorcik V et al. Coupling of plasmonic hot spots with shurikens for superchiral SERS-based enantiomer recognition. *Nanoscale Horiz* **8**, 499–508 (2023).
289. Ran JZ, Li HY, Zhou SX et al. Helical au nanostructure for SERS detection of hazardous molecular and chiral enantiomers. *Food Chem* **458**, 140268 (2024).
290. Jordan MI, Mitchell TM. Machine learning: trends, perspectives, and prospects. *Science* **349**, 255–260 (2015).
291. Asnicar F, Thomas AM, Passerini A et al. Machine learning for microbiologists. *Nat Rev Microbiol* **22**, 191–205 (2024).
292. Carleo G, Cirac I, Cranmer K et al. Machine learning and the physical sciences. *Rev Mod Phys* **91**, 045002 (2019).
293. Jiang SB, Deng WJ, Wang ZS et al. Ka-Band metalens antenna empowered by physics-assisted particle swarm optimization (PA-PSO) algorithm. *Opto-Electron Sci* **3**, 240014 (2024).
294. Ma TG, Wang HZ, Guo LJ. OptoGPT: a foundation model for inverse design in optical multilayer thin film structures. *Opto-Electron Adv* **7**, 240062 (2024).
295. Yin W, Che YX, Li XS et al. Physics-informed deep learning for fringe pattern analysis. *Opto-Electron Adv* **7**, 230034 (2024).
296. Van Houdt G, Mosquera C, Nápoles G. A review on the long short-term memory model. *Artif Intell Rev* **53**, 5929–5955 (2020).
297. Ji WY, Chang J, Xu HX et al. Recent advances in metasurface design and quantum optics applications with machine learning, physics-informed neural networks, and topology optimization methods. *Light Sci Appl* **12**, 169 (2023).
298. Liu C, Ma Q, Luo ZJ et al. A programmable diffractive deep neural network based on a digital-coding metasurface array. *Nat Electron* **5**, 113–122 (2022).
299. Luo XH, Hu YQ, Ou XN et al. Metasurface-enabled on-chip multiplexed diffractive neural networks in the visible. *Light Sci Appl* **11**, 158 (2022).
300. Lin X, Rivenson Y, Yardimci NT et al. All-optical machine learning using diffractive deep neural networks. *Science* **361**, 1004–1008 (2018).
301. Saifullah Y, Wu NX, Wang HP et al. Deep learning in metasurfaces: from automated design to adaptive metadevices. *Adv Photonics* **7**, 034005 (2025).
302. Ma W, Liu ZC, Kudyshev ZA et al. Deep learning for the design of photonic structures. *Nat Photonics* **15**, 77–90 (2021).
303. Akkaş T, Reshadsedghi M, Şen M et al. The role of artificial intelligence in advancing biosensor technology: past, present, and future perspectives. *Adv Mater* **37**, 2504796 (2025).
304. Chen YX, Zhang FY, Dang ZB et al. Chiral detection of biomolecules based on reinforcement learning. *Opto-Electron Sci* **2**, 220019 (2023).

305. Zhang XR, Cui TJ. Artificial intelligence-assisted chiral nanophotonic designs. *Opto-Electron Adv* **6**, 230057 (2023).
306. Richter FU, Sinev I, Zhou SL et al. Gradient high-Q dielectric metasurfaces for broadband sensing and control of vibrational light-matter coupling. *Adv Mater* **36**, 2314279 (2024).
307. John-Herpin A, Tittl A, Kühner L et al. Metasurface-enhanced infrared spectroscopy: an abundance of materials and functionalities. *Adv Mater* **35**, 2110163 (2023).
308. Altug H, Oh SH, Maier SA et al. Advances and applications of nanophotonic biosensors. *Nat Nanotechnol* **17**, 5–16 (2022).
309. Jahani Y, Arvelo ER, Yesilkoy F et al. Imaging-based spectrometer-less optofluidic biosensors based on dielectric metasurfaces for detecting extracellular vesicles. *Nat Commun* **12**, 3246 (2021).
310. Yesilkoy F, Arvelo ER, Jahani Y et al. Ultrasensitive hyperspectral imaging and biodetection enabled by dielectric metasurfaces. *Nat Photonics* **13**, 390–396 (2019).
311. Li DX, Zhou H, Chen ZW et al. Ultrasensitive molecular fingerprint retrieval using strongly detuned overcoupled plasmonic nanoantennas. *Adv Mater* **35**, 2301787 (2023).
312. Li H, Long D, Yuan L et al. Decoupled peak property learning for efficient and interpretable electronic circular dichroism spectrum prediction. *Nat Comput Sci* **5**, 234–244 (2025).
313. An SS, Zheng BW, Shalaginov MY et al. Deep learning modeling approach for metasurfaces with high degrees of freedom. *Opt Express* **28**, 31932–31942 (2020).
314. Luo MC, Xu TJ, Xiao SQ et al. Meta-optics based parallel convolutional processing for neural network accelerator. *Laser Photonics Rev* **18**, 2300984 (2024).
315. Li JL, Telychko M, Yin J et al. Machine vision automated chiral molecule detection and classification in molecular imaging. *J Am Chem Soc* **143**, 10177–10188 (2021).
316. Han JH, Lim YC, Kim RM et al. Neural-network-enabled design of a chiral plasmonic nanodimer for target-specific chirality sensing. *ACS Nano* **17**, 2306–2317 (2023).
317. Zhang N, Gao F, Wang RD et al. Deep-learning empowered customized chiral metasurface for calibration-free biosensing. *Adv Mater* **37**, 2411490 (2025).
318. Visheratina A, Visheratin A, Kumar P et al. Chirality analysis of complex microparticles using deep learning on realistic sets of microscopy images. *ACS Nano* **17**, 7431–7442 (2023).
319. Huang WH, Chu CY, Wu FX et al. Segmentation and morphological handedness classification of chiral materials by deep learning. *J Phys Chem C* **129**, 3690–3697 (2025).
320. Aryal P, Hefner C, Martinez B et al. Microfluidics in environmental analysis: advancements, challenges, and future prospects for rapid and efficient monitoring. *Lab Chip* **24**, 1175–1206 (2024).
321. Lu N, Tay HM, Petchakup C et al. Label-free microfluidic cell sorting and detection for rapid blood analysis. *Lab Chip* **23**, 1226–1257 (2023).
322. Lan ZW, Chen R, Zou D et al. Microfluidic nanoparticle separation for precision medicine. *Adv Sci* **12**, 2411278 (2025).
323. He M, Crow J, Roth M et al. Integrated immunoisolation and protein analysis of circulating exosomes using microfluidic technology. *Lab Chip* **14**, 3773–3780 (2014).
324. Karawdeniya BI, Damry AM, Murugappan K et al. Surface functionalization and texturing of optical metasurfaces for sensing applications. *Chem Rev* **122**, 14990–15030 (2022).
325. Xiao M, Tian F, Liu X et al. Virus detection: from state-of-the-art laboratories to smartphone-based point-of-care testing. *Adv Sci* **9**, 2105904 (2022).
326. Qin XK, Zhong BW, Xu H et al. Manufacturing high-performance flexible sensors via advanced patterning techniques. *Int J Extrem Manuf* **7**, 032003 (2025).
327. Jiang YW, Sima YY, Liu L et al. Research progress on portable electrochemical sensors for detection of mycotoxins in food and environmental samples. *Chem Eng J* **485**, 149860 (2024).
328. Chai HC, Zhu JW, Feng YX et al. Capillarity enabled large-array liquid metal electrodes for compact and high-throughput dielectrophoretic microfluidics. *Adv Mater* **36**, 2310212 (2024).
329. Tan Y, Lu XL, Ding T. Trace-amount detection of chiral molecules based on plasmonic racemic arrays fabricated via direct laser writing. *ACS Sens* **9**, 3290–3295 (2024).
330. García-Guirado J, Svedendahl M, Puigdollers J et al. Enhanced chiral sensing with dielectric nanoresonators. *Nano Lett* **20**, 585–591 (2020).
331. Jia TX, Jeon Y, Feng L et al. Superchirality induced ultrasensitive chiral detection in high-Q optical cavities. *Opto-Electron Adv* **8**, 250079 (2025).


## Acknowledgements

This work was supported by National Key Research and Development Program of China (2023YFF0613600), National Natural Science Foundation of China (62475192, 62205246, 61621001, 62192770, 62192772, 12274296, 62020106009 and 62111530053), Shanghai Pilot Program for Basic Research, Science and Technology Commission of Shanghai Municipality (17JC1400800, 20JC1414600, 21JC1406100 and 22ZR1432400), the "Shu Guang" project supported by Shanghai Municipal Education Commission and Shanghai Education (17SG22), and Fundamental Research Funds for the Central Universities.

## Author contributions

Yuzhi Shi: Conceptualization, Formal analysis, Writing-review & editing, Project administration, Funding acquisition. Chengfeng Li, Xiaolei Lin and Wenwen Xue: Formal analysis, Writing–review & editing. Chengxing Lai, Tao He, Qinghua Song and Zhanshan Wang: Writing-review & editing. Yulan Wang, Din Ping Tsai, Xinbin Cheng and Haidong Zou: Formal analysis, Writing–review & editing, Project administration, Funding acquisition.

## Competing interests

The authors declare no competing financial interests.

**Open Access** This article is licensed under a Creative Commons Attribution 4.0 International License, which permits use, sharing, adaptation, distribution and reproduction in any medium or format, as long as you give appropriate credit to the original author(s) and the source, provide a link to the Creative Commons license, and indicate if changes were made. To view a copy of this license, visit http://creativecommons.org/licenses/by/4.0/
©The Author(s) 2026.
Published by Editorial Office of *Opto-Electronic Advance*, Institute of Optics and Electronics, Chinese Academy of Sciences.

Opto-Electronic Journals Group
www.oejournal.org
Scan for Article PDF